The Reaction Kinetics of Dimethyl Ether. I: High Temperature Pyrolysis and Oxidation in Flow Reactors

S. L. Fischer and F. L. Dryer
Department of Mechanical and Aerospace Engineering,
Princeton University,
Princeton, NJ 08544

H. J. Curran
Chemistry and Materials Science Directorate,
Lawrence Livermore National Laboratory,
Livermore, CA 94551

Accepted to the International Journal of Chemical Kinetics

First submitted on September 3rd 1999,
in final form June 16th 2000.

The Reaction Kinetics of Dimethyl Ether. I: High Temperature Pyrolysis and Oxidation in Flow Reactors

S. L. Fischer and F. L. Dryer
Department of Mechanical and Aerospace Engineering,
Princeton University,
Princeton, NJ 08544

H. J. Curran
Chemistry and Materials Science Directorate,
Lawrence Livermore National Laboratory,
Livermore, CA 94551

Abstract

Dimethyl ether reaction kinetics at high temperature were studied in two different flow reactors under highly dilute conditions. Pyrolysis of dimethyl ether was studied in a variable-pressure flow reactor at 2.5 atmospheres and 1118 K. Studies were also conducted in an atmospheric pressure flow reactor at about 1085 K. These experiments included trace-oxygen-assisted pyrolysis, as well as full oxidation experiments, with the equivalence ratio (ϕ) varying from $0.32 \leq \phi \leq 3.4$. On-line, continuous, extractive sampling in conjunction with Fourier Transform Infra-Red, Non-Dispersive Infra-Red (for CO and CO_2), and electrochemical (for O_2) analyses were performed to quantify species at specific locations along the axis of the turbulent flow reactors. Species concentrations were correlated against residence time in the reactor and species evolution profiles were compared to the predictions of a previously published detailed kinetic mechanism. Some changes were made to the model in order to improve agreement with the present experimental data. However, the revised model continues to reproduce previously reported high temperature jet-stirred reactor and shock tube results.

Introduction

Dimethyl ether (DME) has been featured in the combustion literature as a neat fuel or fuel additive with superior laboratory performance in diesel engines, or as an ignition enhancer for using methanol in diesels [1]–[6]. It has been shown that, compared to neat commercial diesel fuels [4], dimethyl ether addition decreases the emission of CO, NO_x, formaldehyde, particulates and non-methane hydrocarbons, and that DME can be dissolved in diesel fuel in amounts up to 10%. In addition, atmospheric chemistry studies have been performed to address potential effects upon the urban atmosphere (e.g., incremental change in tropospheric ozone levels) of using dimethyl ether as a fuel or fuel additive [7, 8]. DME appears to be environmentally benign in that it does not attack stratospheric ozone, is "virtually non-toxic and non-carcinogenic", is readily degraded in the troposphere, and does not appear to form unstable peroxides upon prolonged exposure to air (as do some higher molecular weight ethers, for example diethyl ether). Potential effects of DME contamination of soil and ground water would appear unlikely, given the high vapor pressure of the material, although we have found no experimental evidence to support such speculation.

High temperature oxidation studies were first published by Dagaut et al. [9], who obtained results in a jet-stirred reactor (1 and 10 atm, $0.2 \leq \phi \leq 2.5$, and $800 \leq T \leq 1300$ K), and by Pfahl and coworkers [10], who measured ignition delay times behind reflected shock waves (13 and 40 bar, $\phi = 1.0$ and $650 \leq T \leq 1300$ K). Both of these studies were used in developing a detailed kinetic mechanism earlier [11].

More recently, Dagaut and co-workers [12] extended their experimental work to include low temperature experiments in a jet-stirred reactor (JSR) and high temperature experiments in a shock tube. Alzueta et al. [13] have also reported oxidation work under flow reactor conditions. Their experiments were performed at atmospheric pressure in the temperature range 600–1500 K and at different air/fuel ratios. Equivalence ratio is defined on the basis of the balanced equation describing the oxidation reaction proper: $3.0 \times [CH_3OCH_3]/[O_2]$. A fuel-lean mixture is one in which the oxidant is in excess, and has an equivalence ratio, $\phi < 1$, while $\phi > 1$ for a fuel-rich mixture. Alzueta et al. focused mainly on the interaction of DME with nitrogen oxides. They found that the oxidation process was promoted in the presence of NO or NO_2. The reaction $\dot{C}H_3 + NO_2 = CH_3\dot{O} + N\dot{O}$, followed by the dissociation of $CH_3\dot{O}$, readily provides H atoms to the system. Similar nitrogen oxide coupling with methyl radicals has also been reported for methane oxidation [14]. None of the available data described above include studies on the high temperature pyrolysis of DME, although the unimolecular decomposition of DME is known to be relatively fast at high temperatures.

The experimental research at Princeton was initiated principally to further understanding of the low and intermediate temperature behavior of DME oxidation. However, hot ignition and transition to high temperature kinetic behavior are strongly influenced by the high temperature kinetic aspects of the mechanism. We therefore conducted experiments and modeling studies at high temperatures, including pyrolysis studies as a pre-requisite to the intermediate and low temperature work, and we report the results of these high temperature studies here. In a companion paper [15], we address the low and intermediate temperature kinetic issues and compare them with a kinetic model that includes the higher temperature kinetic aspects developed in this paper. There we report new experimental observations, not noted in prior intermediate temperature experiments that require significant modifications in the low and intermediate temperature mechanism developed earlier.

Experimental

Flow reactor experiments typically provide data in a range of conditions not accessible to shock tubes, stirred reactors, and static reactors. Two different flow reactors were used in the present work, an atmospheric pressure flow reactor (APFR), and a variable-pressure flow reactor (VPFR).

The high temperature, atmospheric pressure flow reactor (APFR) is fully documented in the literature in numerous papers (e.g., Crocco et al. [16], Yetter et al. [17] and Roesler et al. [18]), and is only briefly described here. The carrier gas is a turbulent flow of pre-heated nitrogen into which oxygen and water vapor are injected and pre-mixed to dilute amounts ($\approx 1\%$ by volume). Reactant concentrations are typically diluted sufficiently that the total heat release in the reaction zone is no more than 100 K. Fuel vapor diluted in nitrogen is injected into the carrier mixture at the throat of a converging-diverging nozzle section. The reactants subsequently mix within the quartz diffuser section, and a quasi-steady reaction is established along the length of a constant-diameter quartz test section downstream of the

diffuser. This test section is 10.16 cm in diameter and approximately 1 m long. The reaction is maintained effectively adiabatic with the use of electric resistance heaters and insulation material surrounding the entire reactor. At very dilute conditions and with some reaction systems, heat release over the length of the reaction zone is so small that the flow can be treated as isothermal rather than adiabatic. Data are obtained using a relocatable probe, consisting of a stainless steel, hot water-cooled gas sampling probe and a Pt/Pt-13% Rh thermocouple probe. The thermocouple junction is coated with silica to prevent catalytic reactions on the thermocouple surface. Relocating the axial position of the sampling probe varies the reaction time (distance between the point of mixing and the sampling location). Other features regarding experimental procedures and analytical measurements common to both reactors are described in more detail below.

The majority of experiments reported here and in the companion paper [15] were performed in the VPFR, Fig. 1. The VPFR can access a wide range of conditions: temperature (550-1200 K); pressure (0.3–20 atm); and equivalence ratio (pure pyrolysis to oxygen-rich conditions). A novel design feature of the VPFR (in comparison to the APFR and other flow reactors reported in the literature) is based on fixing the diagnostic sampling position and moving the point of fuel injection relative to this location to vary the reaction time. The concept is similar to that often pursued in low pressure, fast flow reactors and in the study of pre-mixed, laminar, one-dimensional flames where the burner, rather than the diagnostic sampling position, is moved. This design accommodates very short gas sampling residence times to continuous, on-line diagnostic instruments (important for on-line measurement of low-stability molecular species such as aldehydes, acids, or other oxygenates), and simpler optical access for in-situ diagnostics at the sampling location [24, 27]. The relative length of the reaction zone (from mixing point to sampling point) introduces significant coupling in terms of boundary heat transfer, particularly if the reaction is significantly exothermic or endothermic. In order to deal with these issues effectively, all experimental parameters must be independently closed-loop controlled. These controls permit the initial reaction, wall boundary conditions, and reaction pressure to be reproduced accurately upon relocations of the mixer relative to the diagnostic location (to change reaction time).

In the VPFR, oxidizer is added to the nitrogen carrier gas (flowing from left to right) which is pre-heated to the desired initial reaction temperature using a composite ferrous-alloy/tungsten electrical resistance heater. For pyrolysis studies, no oxidizer is added, and the sealed nature of the device permits background levels of as little as 10 ppm to be obtained (This is the typical background levels of oxygen in the liquid nitrogen-based gas supply source). Pre-vaporized dimethyl ether, along with about 5–10% of the total nitrogen carrier flow, is injected into the carrier-oxidizer stream at the entrance to a mixer-diffuser, Fig. 1, through a multi-jet injector. The upstream carrier flow is directed outward to the reactor tube wall by a central baffle plate, and then radially inward through a gap between the baffle plate and the mixer-diffuser block. A large number of opposed jets of the pre-vaporized fuel/nitrogen mixture issue into this radial inward flow from the fuel injection probe. An opposed-jet stirring occurs at the entrance to the diffuser section, with a nominal turnover time of about 0.5% of the total reaction test time downstream of the diffuser. The ability of the VPFR design to achieve rapid mixing of reactants and a quasi-steady initial reaction temperature have been experimentally demonstrated elsewhere [24].

The mixer-diffuser, Fig. 1, is approximately 45 cm long and is machined from a low

porosity, silica foam block to an outside diameter about 1.2 mm less than the nominal 10.16 cm inside diameter of the cylindrical reactor duct. The interior contour of the diffuser section has a throat diameter of 2.5 cm and an expansion half-angle of 5 degrees. The central baffle plate upstream of the mixer-diffuser is lined with fused silica to minimize chemical surface effects that might occur in the mixing region. A stepper-motor-driven mechanism inside the pressure boundary is used to position the mixer-diffuser by moving the fuel injector. Dimethyl ether was pre-vaporized and mixed with nitrogen at the entrance to the fuel injector.

The pressure shell of the VPFR, Fig. 1, is made of 12-inch Schedule 40 carbon steel pipe and is ASME code stamped for operation from full vacuum to 28 atm and 245–533 K shell temperature. The cylindrical reactor section in which kinetic measurements are performed is a 173 cm long, 2 mm wall thickness, 10.16 cm inside diameter, fused silica tube, in which the silica mixer block can be moved. A maximum of about 115 cm and a minimum of 25 cm of axial distance from the throat of the mixer-diffuser section to the sampling position are possible.

In both reactors, reactants are typically diluted in large amounts of pre-heated nitrogen. Dilution reduces the experimentally observed reaction rates from those found under higher concentration conditions, for example stoichiometric conditions in air. Thus, the reaction times evident in combustion systems (often less than a few milliseconds) are scaled by dilution to a range of reaction times from 1.0×10^{-3} to 2.0 seconds. By maintaining large convective rates for these dilute conditions, the effects of axial diffusive transport are rendered negligible. Radial uniformity in the species and temperature profiles at each axial location are produced by developing, turbulent flow conditions. Wall collisional effects are of minimal importance because the time for molecules to diffuse to and from the wall to affect the core flow are long, in comparison to the mean residence time of the flow in the reactor. As a result of the laminarized flow near the wall, this can be true even with the presence of enhanced diffusivities from turbulence in the core flow. Both our own studies and those of Seeley et al. [19] have demonstrated this last point. Surface effects in the mixing region can occur, and along with mixing phenomena, influence the reaction initiation process. Although local concentration fluctuations remain a source of turbulence/chemistry coupling, determinations of elementary reaction rates (e.g., Hochgreb and Dryer [20], Yetter and Dryer [21], Allen et al. [22], and Mueller et al. [23]) from our data suggest that turbulence/chemistry coupling perturbations from local concentration fluctuations are within the uncertainties of the kinetic measurements themselves.

The flows in both reactors are "developing" ones, with boundary-layer growth occurring at the reactor walls, over the length of the reaction region. The axial velocity distribution in each reactor was defined experimentally using cold-flow conditions and pitot pressure probes, as well as hot wire anemometry. These measurements are then related to experimental hot-flow conditions through Reynolds number correlations (e.g., Held [24]). Relative times of various axial positions to one another and to the point of the mixing location are defined by integrating the velocity distribution function along the axial coordinate.

Each flow reactor was operated as a steady, isobaric flow device. In both the APFR and VPFR, experiments were performed at constant initial reaction temperature and initial reactant concentrations, while the reaction time was varied by changing the distance from mixing to sampling locations. Thus, one obtains a reactant/intermediate and reaction

temperature profiles as functions of residence time under near-adiabatic conditions. In the VPFR, another type of experiment was also performed. For a constant reaction time, initial reactant concentrations were held constant, and the initial reaction temperature was varied, generating so-called "reactivity" profiles. This mode of operation is more fully described in [25, 26].

In each type of experiment described above, the heat transfer and sampling systems, Fig. 2, are given time to reach quasi-steady conditions prior to sampling and diagnostic data acquisition. All of the independent experimental parameters (nitrogen carrier, liquid fuel, fuel vapor nitrogen diluent, and oxidizer flows; carrier inlet, reactor wall temperatures; mixing location relative to sampling location; and for the VPFR, reaction pressure) are monitored. In the APFR experiments, these monitoring processes are performed manually, while in the VPFR all parameters are electronically monitored and independently controlled from a single microprocessor-based control station.

A hot-water-cooled, wall-convection-quenched, stainless steel sample probe was used in both the APFR and VPFR to continuously extract and convectively quench a small portion of the reacting gases. The continuous sample was extracted from an axial location in the flow. The reaction temperature at the gas sampling location was measured with a silica coated Pt-13%Rh/Pt thermocouple (3 K uncertainty). Calculated gas sampling quenching times have been estimated to be very short in comparison to overall reaction times (Dryer [28] and Emdee [29]).

The sampled flow passed through heated sampling lines to a Nicolet Model 730 FTIR, equipped with a 0.7 liter, 10 meter multi-reflective cell, Fig. 2. The cell pressure (760 mm Hg) and temperature (100°C) were held constant for all measurements. The analytical flow exiting the cell was then directed to a continuous flow electrochemical analyzer for O_2, to continuous non-dispersive infrared (NDIR) analyzers for CO and CO_2, and to a continuous selective detector for H_2. All of the FTIR spectra are multi scan-averaged (32 scans), and computer storage of the raw spectral data permit searches for additional information (and species), even after the experiment has been performed. Data acquired by all of the above instruments were recorded on a hard disk-based microprocessor system and post-processed to obtain species concentrations.

The FTIR utilized a liquid nitrogen-cooled MCT-A detector to measure spectral absorbance with a resolution down to 0.125 cm^{-1}. Multivariate least squares fit software is used for quantification of the spectral data. Calibrations for species are obtained by measuring absorbance for different concentrations of each compound in nitrogen (and in mixtures in nitrogen), or by comparing responses to that determined by conversion of the material to combustion products. For each species with the exceptions of formic acid (HOCHO) and water, species concentration was determined from spectral features that were isolated from interference produced by other species. Formic acid and water spectra interference could not be completely separated, and a multi-component absorbance calibrations had to be performed for these two species. FTIR species concentration uncertainties were as follows: CH_3OCH_3 (4% or $<$ 50 ppm), CH_4 (2%), CH_3OH (2%), C_2H_6 (2%), C_2H_4 (2%), CH_2O (5% or $<$ 10 ppm), HOCHO (3.5% or $<$ 12 ppm), H_2O (10%). Other analytical measurements had uncertainties as follows: O_2 (3%); CO (2%); CO_2 (2%). No other hydrocarbon species ($>$ 1 ppm) were detected in the experiments reported here or in the companion paper.

Computational Modeling

All of the modeling computations in this study were carried out using the HCT modeling code [30]. The fundamental modeling assumptions used in comparing the kinetic calculations with experiments are as follows:

Flow reactor: Constant pressure, adiabatic, zero-dimensional. The constant pressure assumption is essentially a low Mach number assumption. As noted above, adiabaticity is approximated in the experiments through the use of preheated reactor tube walls and a short length to diameter ratio in the reactor tube. Experimentally, axial diffusion is negligible only where the characteristic diffusion length is much greater than the convective length. Although this assumption is reasonably valid over much of the reaction zone, it breaks down in regions of high concentration gradients, such as in the rapid transition in the oxidation rate of CO accompanying the depletion of hydrocarbon species (e.g. see Fig. 11). Furthermore, the finite-rate mixing of fuel and oxidizer, and potentially, small recirculation zones near the mixing region, all result in uncertainty in specification of an absolute "zero time" for flow reactor experiments. Modeling simulation of these effects using stirred reactor-plug flow coupled models has shown that they all serve to translate the calculated species and temperature profiles along the time axis toward the origin [24]. Constant initial condition calculations using the mechanism reported here also show that initial perturbations of the system are quickly relaxed and result in no historical effects downstream, other than shifting the entire reaction profiles (without perturbations) with respect to the "zero time". Similar observations have been shown by others for the CO/hydrogen/oxygen, and methanol systems [24, 31]. Thus, for these reaction systems, when the calculated species versus time profiles are artificially temporally aligned at an arbitrary reference point within the downstream reaction zone where fuel disappearance is observed, the calculations and experimental profiles overlay one another nearly perfectly. This result must be verified for each reaction system in question, particularly for those such as dimethyl ether, in which unimolecular decomposition may contribute to the overall fuel disappearance in the post induction region.

In comparing calculations with species-time experimental data, the time axis of the data was effectively "translated" to match a particular extent of reaction between the experimental and computed results. "Time shifting" and the results achieved by the above approach are entirely consistent with the assumption (noted above) that within the range of extents of reaction to be compared with the calculation, axial diffusion time scales are much longer than kinetic and convective time scales and include the conceptual assumption that induction chemistry does not substantially influence the important initial conditions for the post-induction chemistry. Mathematically, the solution of the conservation equations for the post induction region then becomes an initial value problem, and any single matching point between the experiment and computation is equivalent. Computationally, calculations can be marched upstream or downstream from a matching point, without concern, and all matching points are equivalent. Here we matched the points of 50% observed fuel disappearance to compare calculation and experiment.

On the other hand, comparing reactivity profiles with calculations raises concerns with "time shifting" approaches, for the comparisons include variations in the initial temperature. This issue is discussed in more detail in the companion paper, where these types of experiments in the VPFR are reported and discussed.

Shock tubes: The thermal environment in the post-shock region can be safely assumed to be adiabatic. Also, the short reaction time scales relative to diffusive times permits the zero-dimensional approximation. The treatment of the free boundary of the reaction zone is open to some debate. A limiting case, frequently applied and used in this study, assumes a constant-volume (density) boundary, which implies that the bulk expansion of the fluid due to temperature rise and average molecular weight change overwhelms the inertial effects of the surrounding fluid. However, the situation is rarely as clear-cut as the simplified model would indicate.

Stirred Reactors: The jet-stirred reactor is simulated as a homogeneous, constant volume reactor which is assumed to be at constant temperature and pressure, with a prescribed influx of fresh reactants such that the residence time is constant within the reactor.

The detailed chemical kinetic reaction mechanism used in these calculations was based on the hierarchical nature [32] of reacting systems, starting with a core mechanism describing H_2/O_2 and CO oxidation. To this is added the progressively larger C_1–C_2 mechanism and ultimately the DME mechanism, whereby the complete model consists of 82 different chemical species and 351 elementary reactions. The dimethyl ether reaction mechanism is listed in Table 1.

The thermodynamic properties for the relevant radicals and stable parents were obtained by group additivity using THERM [33] with updated H/C/O groups and bond dissociation groups [34]. The thermochemical data, listed in Table 2, allow the calculation of reverse reaction rate constants by microscopic reversibility. Our previous version of the dimethyl ether mechanism is provided in reference [11]. This, in combination with the changes documented in the present paper, comprises the updated mechanism. An electronic version of the updated mechanism can be obtained by electronic mail in either HCT or CHEMKIN format by writing to the authors (fldryer@phoenix.princeton.edu).

At high temperatures, the fuel consumption pathway is quite simple, with unimolecular decomposition of the fuel, reaction (273), producing methoxy and methyl radicals, and β–scission of the methoxymethyl radical, reaction (282), yielding formaldehyde and a methyl radical. At high temperatures, the methoxy radical undergoes β-scission to yield formaldehyde and a hydrogen atom. Therefore, the hydrogen and methane submechanisms and, in particular, the formaldehyde submechanism are important sub-sets of the dimethyl ether oxidation system.

In this study, the hydrogen submechanism is based on that which has recently been validated by Mueller et al. [35] against experimental data in a flow reactor over a pressure and temperature range of 0.3 to 15.7 atm and 850–1040 K, respectively. These data span the explosion limit behavior of the system and place particular emphasis on $H\dot{O}_2$ and H_2O_2 kinetics. The H_2 submechanism used here produces, within experimental error, identical simulated results to those depicted in the Mueller publication. It is currently impossible for both HCT and CHEMKIN mechanisms to be exactly the same as the format used for the thermodynamic parameters of species are different in both codes.

The formaldehyde submechanism is based on the experimental and modeling work of Hochgreb et al. [36, 37]. Some changes have been made to hydrogen atom abstraction reactions from formaldehyde by radical species and these are detailed in our analysis below. A comparison of the model-predicted intermediate profiles versus experimental data for a limited set of formaldehyde oxidation results is provided in Figs. 3–5. Overall there is

excellent agreement between model and experiment. The methane submechanism, Table 1, was validated by comparisons with the previously published data of Amano and Dryer [14], with very good agreement observed between model and experiment. Figure 6 is an example of a comparison between simulation and experiment.

By performing an initial validation on the hydrogen, formaldehyde, and methane submechanisms, we are confident that any changes in rate constant expressions necessary to simulate both pyrolysis and oxidation data on dimethyl ether are a part of the dimethyl ether mechanism itself and not part of these submechanism.

	Reaction	$\mathcal{A}$	n	$\mathcal{E}_a$	Reference
1.	$CH_3 + H(+M) = CH_4(+M)$	2.14E + 15	−0.40	0.	[38]
	Low pressure limit	3.31E + 30	−4.00	2108.	
	Troe parameters a=0.0,				
	T*** = 1.0E−15, T* = 1.0E−15, T** = 40.				
	Enhanced Third Body Efficiencies:				
	H_2 = 2.0, H_2O = 5.0, CO = 2.0, CO_2 = 3.0				
2.	$CH_4 + H = CH_3 + H_2$	1.73E + 04	3.00	8224.	[39]
3.	$CH_4 + OH = CH_3 + H_2O$	1.93E + 05	2.40	2106.	[40]
4.	$CH_4 + O = CH_3 + OH$	2.13E + 06	2.21	6480.	[41]
5.	$C_2H_6 + CH_3 = C_2H_5 + CH_4$	1.51E − 07	6.00	6047.	[42]
6.	$HCO + OH = CO + H_2O$	1.02E + 14	0.00	0.	[42]
7.	$CO + OH = CO_2 + H$	1.40E + 05	1.95	−1347.	[35]
8.	$H + O_2 = O + OH$	1.97E + 14	0.00	16540.	[43]
9.	$O + H_2 = H + OH$	5.08E + 04	2.67	6292.	[44]
10.	$O + H_2O = OH + OH$	2.97E + 06	2.02	13400.	[45]
11.	$OH + H_2 = H + H_2O$	2.16E + 08	1.51	3430.	[46]
12.	$HCO + M = H + CO + M$	1.86E + 17	−1.00	17000.	[47]
	Enhanced Third Body Efficiencies:				
	H_2 = 2.5, H_2O = 12.0, CO = 1.9, CO_2 = 3.8				
13.	$H_2O_2 + OH = H_2O + HO_2$	1.00E + 12	0.00	0.	[48]
14.	$C_2H_4 + O = CH_3 + HCO$	1.02E + 07	1.88	179.	[40]
15.	$H + C_2H_4(+M) = C_2H_5(+M)$	1.08E + 12	0.34	1822.	[38]
	Low pressure limit	1.11E + 34	−5.00	4448.	
	Troe parameters a=1.0,				
	T*** = 1.0E−15, T* = 95., T** = 200.				
	Enhanced Third Body Efficiencies:				
	H_2 = 2.0, H_2O = 5.0, CO = 2.0, CO_2 = 3.0				
16.	$CH_3OH(+M) = CH_3 + OH(+M)$	1.90E + 16	0.00	91730.	[49]
	Low pressure limit	2.95E + 30	−7.35	95460.	
	Troe parameters a=0.414,				
	T*** = 279., T* = 5459., T** = 1.0E+100.				
	Enhanced Third Body Efficiencies:				
	H_2 = 2.0, H_2O = 16.0, CO = 2.0, CO_2 = 3.0				
17.	$C_2H_6 + H = C_2H_5 + H_2$	5.54E + 02	3.50	5167.	[40]

18.	$CH_3OH + HO_2 = CH_2OH + H_2O_2$	3.98E + 13	0.00	19400.	[50]
19.	$C_2H_5 + O_2 = C_2H_4 + HO_2$	1.22E + 30	−5.76	10100.	[51]
20.	$C_2H_6 + OH = C_2H_5 + H_2O$	5.12E + 06	2.06	855.	[52]
21.	$C_2H_6 + O = C_2H_5 + OH$	1.13E + 14	0.00	7850.	[53]
22.	$CH_3 + HO_2 = CH_3O + OH$	1.10E + 13	0.00	0.	[14]
23.	$CO + HO_2 = CO_2 + OH$	3.01E + 13	0.00	23000.	[35]
24.	$CH_3 + CH_3(+M) = C_2H_6(+M)$	9.21E + 16	−1.17	635.8	[54]
	Low pressure limit	1.14E + 36	−5.246	1705.	
	Troe parameters a=0.405,				
	T^{***} = 1120., T^{*} = 69.6, T^{**} = 1.0E+100.				
	Enhanced Third Body Efficiencies:				
	H_2 = 2.0, H_2O = 5.0, CO = 2.0, CO_2 = 3.0				
25.	$H + OH + M = H_2O + M$	2.25E + 22	−2.00	0.	[40]
	Enhanced Third Body Efficiencies:				
	H_2 = 2.5, H_2O = 12.0, CO = 1.9, CO_2 = 3.8				
26.	$H + O_2(+M) = HO_2(+M)$	1.48E + 12	0.60	0.	[35]
	Low pressure limit	3.50E + 16	−0.41	−1116.	
	Troe parameters a=0.5,				
	T^{***} = 1.0E−30, T^{*} = 1.0E+30, T^{**} = 1.0E+100.				
	Enhanced Third Body Efficiencies:				
	H_2 = 2.0, H_2O = 5.0, CO = 2.0, CO_2 = 3.0				
27.	$CO + O(+M) = CO_2(+M)$	1.80E + 10	0.00	2384.	[35]
	Low pressure limit	1.35E + 24	−2.79	4191.	
	Enhanced Third Body Efficiencies:				
	H_2 = 2.5, H_2O = 12.0, CO = 1.9, CO_2 = 3.8				
28.	$CO + O_2 = CO_2 + O$	1.07E − 15	7.13	13320.	† [a]
29.	$HCO + H = CO + H_2$	7.34E + 13	0.00	0.	[55]
30.	$HCO + O = CO + OH$	3.02E + 13	0.00	0.	[40]
31.	$HCO + H + M = CH_2O + M$	2.66E + 24	−2.57	427.	[56]
32.	$CH_2O + OH = HCO + H_2O$	3.43E + 09	1.18	−447.	[40]
33.	$CH_2O + H = HCO + H_2$	9.33E + 08	1.50	2976.	† [b]
34.	$CH_2O + O = HCO + OH$	6.26E + 09	1.15	2260.	† [a]
35.	$CH_3 + OH = CH_2O + H_2$	2.25E + 13	0.00	4300.	[57]
36.	$CH_3 + O = CH_2O + H$	8.00E + 13	0.00	0.	[58]
37.	$CH_3 + O_2 = CH_3O + O$	2.00E + 18	−1.57	29230.	[40]
38.	$CH_2O + CH_3 = HCO + CH_4$	3.64E − 06	5.42	998.	† [a]
39.	$HCO + CH_3 = CH_4 + CO$	1.21E + 14	0.00	0.	[40]
40.	$CH_3O(+M) = CH_2O + H(+M)$	5.45E + 13	0.00	13500.	[59]
	Low pressure limit	2.34E + 25	−2.70	30600.	
41.	$C_2H_4(+M) = C_2H_2 + H_2(+M)$	2.60E + 17	0.00	79350.	[60]
	Low pressure limit	1.50E + 15	0.00	55443.	
42.	$HO_2 + O = OH + O_2$	3.25E + 13	0.00	0.	[61]
43.	$CH_2O + O_2 = HCO + HO_2$	2.05E + 13	0.00	38950.	[40]

44.	$CH_3O + O_2 = CH_2O + HO_2$	5.50E + 10	0.00	2424.	† [a]
45.	$CH_3 + HO_2 = CH_4 + O_2$	3.00E + 12	0.00	0.	[14]
46.	$HCO + O_2 = CO + HO_2$	7.58E + 12	0.00	410.	[62]
47.	$HO_2 + H = OH + OH$	7.08E + 13	0.00	300.	[35]
48.	$HO_2 + H = H_2 + O_2$	1.66E + 13	0.00	820.	[35]
49.	$HO_2 + OH = H_2O + O_2$	2.89E + 13	0.00	−500.	[61]
50.	$HO_2 + HO_2 = H_2O_2 + O_2$	4.20E + 14	0.00	11980.	[63]
51.	$OH + OH(+M) = H_2O_2(+M)$	1.24E + 14	−0.37	0.	[64]
	Low pressure limit	3.04E + 30	−4.63	2049.	
	Troe parameters a=0.47,				
	$T^{***} = 100.$, $T^{*} = 2000.$, $T^{**} = 1.0E{+}15.$				
	Enhanced Third Body Efficiencies:				
	$H_2 = 2.5$, $H_2O = 12.0$, $CO = 1.9$, $CO_2 = 3.8$				
52.	$H_2O_2 + H = H_2O + OH$	2.41E + 13	0.00	3970.	[40]
53.	$CH_4 + HO_2 = CH_3 + H_2O_2$	3.42E + 11	0.00	19290.	† [a]
54.	$CH_2O + HO_2 = HCO + H_2O_2$	5.82E − 03	4.53	6557.	[65]
55.	$O + H + M = OH + M$	4.72E + 18	−1.00	0.	[40]
	Enhanced Third Body Efficiencies:				
	$H_2 = 12.5$, $H_2O = 12.0$, $CO = 1.9$, $CO_2 = 3.8$				
56.	$O + O + M = O_2 + M$	6.17E + 15	−0.50	0.	[40]
	Enhanced Third Body Efficiencies:				
	$H_2 = 12.5$, $H_2O = 12.0$, $CO = 1.9$, $CO_2 = 3.8$				
57.	$H_2 + M = H + H + M$	4.57E + 19	−1.40	104400.	[40]
	Enhanced Third Body Efficiencies:				
	$H_2 = 2.5$, $H_2O = 12.0$, $CO = 1.9$, $CO_2 = 3.8$				
58.	$C_2H_3 + H(+M) = C_2H_4 + (M)$	6.10E + 12	0.27	280.	[38]
	Low pressure limit	9.80E + 29	−3.86	3320.	
	Troe parameters a=0.782,				
	$T^{***} = 208.$, $T^{*} = 2663.$, $T^{**} = 6095.$				
	Enhanced Third Body Efficiencies:				
	$H_2 = 2.0$, $H_2O = 5.0$, $CO = 2.0$, $CO_2 = 3.0$				
59.	$C_2H_5 + C_2H_3 = C_2H_4 + C_2H_4$	3.00E + 12	0.00	0.	[66]
60.	$C_2H_2 + H(+M) = C_2H_3(+M)$	3.11E + 11	0.58	2589.	[38]
	Low pressure limit	2.25E + 40	−7.27	6577.	
	Troe parameters a=1.0,				
	$T^{***} = 1.0E{-}15$, $T^{*} = 675.$, $T^{**} = 1.0E{+}15.$				
	Enhanced Third Body Efficiencies:				
	$H_2 = 2.0$, $H_2O = 5.0$, $CO = 2.0$, $CO_2 = 3.0$				
61.	$C_2H_4 + H = C_2H_3 + H_2$	8.42E − 03	4.62	2583.	† [a]
62.	$C_2H_4 + OH = C_2H_3 + H_2O$	2.05E + 13	0.00	5955.	[67]
63.	$C_2H_3 + O_2 = C_2H_2 + HO_2$	5.19E + 15	−1.26	3310.	[58]
64.	$C_2H_2 + M = C_2H + H + M$	4.20E + 16	0.00	107000.	[38]
65.	$C_2H_2 + O_2 = HCCO + OH$	2.00E + 08	1.50	30100.	[68]

66.	$C_2H_2 + O_2 = CO + H_2O$	7.28E + 19	−2.54	1809.	[38]
67.	$C_2H_2 + OH = C_2H + H_2O$	3.39E + 07	2.00	14000.	[68]
68.	$O + C_2H_2 = C_2H + OH$	3.20E + 15	−0.60	15000.	[68]
69.	$C_2H_2 + O = CH_2 + CO$	6.12E + 06	2.00	1900.	[38]
70.	$C_2H + O_2 = HCO + CO$	2.41E + 12	0.00	0.	[40]
71.	$C_2H + O = CO + CH$	1.81E + 13	0.00	0.	[40]
72.	$CH_2 + O_2 = HCO + OH$	1.29E + 20	−3.30	284.	[38]
73.	$CH_2 + O = CO + H + H$	5.00E + 13	0.00	0.	[68]
74.	$CH_2 + H = CH + H_2$	1.00E + 18	−1.56	0.	[68]
75.	$CH_2 + OH = CH + H_2O$	1.13E + 07	2.00	3000.	[68]
76.	$CH_2 + O_2 = CO_2 + H + H$	3.29E + 21	−3.30	2868.	[38]
77.	$CH + O_2 = HCO + O$	3.30E + 13	0.00	0.	[68]
78.	$CH_3OH + OH = CH_2OH + H_2O$	7.10E + 06	1.80	−596.	[69]
79.	$CH_3OH + H = CH_3O + H_2$	3.60E + 12	0.00	6095.	[70]
80.	$CH_3OH + H = CH_2OH + H_2$	1.44E + 13	0.00	6095.	[70]
81.	$CH_3OH + CH_3 = CH_2OH + CH_4$	3.19E + 01	3.17	7172.	[71]
82.	$CH_3OH + O = CH_2OH + OH$	3.88E + 05	2.50	3080.	[71]
83.	$CH_2OH + O_2 = CH_2O + HO_2$	3.81E + 06	2.00	1640.	† [a]
84.	$CH_2OH(+M) = CH_2O + H + (M)$	2.80E + 14	−0.73	32820.	[49]
	Low pressure limit	6.01E + 33	−5.39	36200.	
	Troe parameters a=0.96,				
	$T^{***} = 67.6$, $T^{*} = 1855.$, $T^{**} = 7543.$				
	Enhanced Third Body Efficiencies:				
	$H_2 = 2.0$, $H_2O = 5.0$, $CO = 2.0$, $CO_2 = 3.0$				
85.	$C_2H_3 + O_2 = C_2H_2 + HO_2$	2.12E − 06	6.00	9484.	[38]
86.	$H_2O_2 + O = OH + HO_2$	9.55E + 06	2.00	3970.	[40]
87.	$C_2H_2 + O = HCCO + H$	1.43E + 07	2.00	1900.	[38]
88.	$C_2H_2 + OH = CH_2CO + H$	3.24E + 13	0.00	12000.	[72]
89.	$CH_2CO + H = CH_3 + CO$	1.13E + 13	0.00	3428.	[73]
90.	$CH_2CO + O = CH_2 + CO_2$	1.75E + 12	0.00	1350.	[58]
91.	$CH_2 + O2 = CH_2O + O$	3.29E + 21	−3.30	2868.	[38]
92.	$CH_2CO(+M) = CH_2 + CO(+M)$	3.00E + 14	0.00	70980.	[68]
	Low pressure limit	3.60E + 15	0.00	59270.	
93.	$CH_2CO + O = HCCO + OH$	1.00E + 13	0.00	8000.	[68]
94.	$CH_2CO + OH = HCCO + H_2O$	1.00E + 13	0.00	3000.	[38]
95.	$CH_2CO + H = HCCO + H_2$	2.00E + 14	0.00	8000.	[68]
96.	$HCCO + OH = HCO + HCO$	1.00E + 13	0.00	0.	[66]
97.	$HCCO + H = CH_2(S) + CO$	1.10E + 14	0.00	0.	[68]
98.	$HCCO + O = H + CO + CO$	8.00E + 13	0.00	0.	[74]
99.	$C_2H_6 + O_2 = C_2H_5 + HO_2$	4.00E + 13	0.00	50900.	† [c]
100.	$C_2H_6 + HO_2 = C_2H_5 + H_2O_2$	1.70E + 13	0.00	20460.	† [d]
101.	$CH_2 + O_2 = CO_2 + H_2$	1.01E + 21	−3.30	1508.	[38]
102.	$CH_3 + C_2H_3 = CH_4 + C_2H_2$	3.92E + 11	0.00	0.	[40]

103.	$CH_3 + C_2H_5 = CH_4 + C_2H_4$	1.95E + 13	−0.50	0.	[40]
104.	$CH_3O + CH_3O = CH_3OH + CH_2O$	6.03E + 13	0.00	0.	[40]
105.	$CH_2O + CH_3O = CH_3OH + HCO$	1.15E + 11	0.00	1280.	[66]
106.	$CH_4 + CH_3O = CH_3 + CH_3OH$	1.57E + 11	0.00	8843.	[40]
107.	$C_2H_6 + CH_3O = C_2H_5 + CH_3OH$	3.00E + 11	0.00	7000.	[66]
108.	$C_2H_3 + H = C_2H_2 + H_2$	2.00E + 13	0.00	2500.	[66]
109.	$CH_3O + CH_3OH = CH_2OH + CH_3OH$	3.00E + 11	0.00	4074.	[40]
110.	$CH_3OH + OH = CH_3O + H_2O$	1.00E + 06	2.10	497.	[69]
111.	$C_2H_5 + H = CH_3 + CH_3$	3.61E + 13	0.00	0.	[42]
112.	$C_2H_3 + O_2 = CH_2O + HCO$	1.70E + 29	−5.31	6500.	[58]
113.	$C_2H_5 + H = C_2H_6$	3.61E + 13	0.00	0.	[75]
114.	$C_2H_5OH(+M) = CH_2OH + CH_3(+M)$	5.71E + 23	−1.68	94405.	[76]
	Low pressure limit	3.11E + 85	−18.84	113100.	
	Troe parameters a=0.5,				
	$T^{***} = 550.$, $T^{*} = 825.$, $T^{**} = 6100.$				
	Enhanced Third Body Efficiencies:				
	$H_2 = 2.0$, $H_2O = 5.0$, CO = 2.0, $CO_2 = 3.0$				
115.	$C_2H_5OH(+M) = C_2H_5 + OH(+M)$	2.40E + 23	−1.62	99535.	[76]
	Low pressure limit	5.11E + 85	−18.8	118770.	
	Troe parameters a=0.5,				
	$T^{***} = 650.$, $T^{*} = 800.$, $T^{**} = 1.0E{+}15.$				
	Enhanced Third Body Efficiencies:				
	$H_2 = 2.0$, $H_2O = 5.0$, CO = 2.0, $CO_2 = 3.0$				
116.	$C_2H_5OH(+M) = C_2H_4 + H_2O(+M)$	2.79E + 13	0.09	66136.	[76]
	Low pressure limit	2.57E + 83	−18.85	86453.	
	Troe parameters a=0.7,				
	$T^{***} = 350.$, $T^{*} = 800.$, $T^{**} = 380.$				
	Enhanced Third Body Efficiencies:				
	$H_2 = 2.0$, $H_2O = 5.0$, CO = 2.0, $CO_2 = 3.0$				
117.	$C_2H_5OH(+M) = CH_3CHO + H_2(+M)$	7.42E + 11	0.10	91007.	[76]
	Low pressure limit	4.46E + 87	−19.42	115590.	
	Troe parameters a=0.9,				
	$T^{***} = 900.$, $T^{*} = 1100.$, $T^{**} = 3500.$				
	Enhanced Third Body Efficiencies:				
	$H_2 = 2.0$, $H_2O = 5.0$, CO = 2.0, $CO_2 = 3.0$				
118.	$C_2H_5OH + O_2 = pC_2H_4OH + HO_2$	2.00E + 13	0.00	52800.	† [c]
119.	$C_2H_5OH + O_2 = sC_2H_4OH + HO_2$	1.50E + 13	0.00	50150.	† [c]
120.	$C_2H_5OH + OH = pC_2H_4OH + H_2O$	1.74E + 11	0.27	600.	[76]
121.	$C_2H_5OH + OH = sC_2H_4OH + H_2O$	4.64E + 11	0.15	0.	[76]
122.	$C_2H_5OH + H = pC_2H_4OH + H_2$	1.23E + 07	1.80	5098.	[76]
123.	$C_2H_5OH + H = sC_2H_4OH + H_2$	2.58E + 07	1.65	2827.	[76]
124.	$C_2H_5OH + HO_2 = pC_2H_4OH + H_2O_2$	1.23E + 04	2.55	15750.	[76]
125.	$C_2H_5OH + HO_2 = sC_2H_4OH + H_2O_2$	8.20E + 03	2.55	10750.	[76]

126.	$C_2H_5OH + HO_2 = C_2H_5O + H_2O_2$	2.50E + 12	0.00	24000.	[76]
127.	$C_2H_5OH + O = pC_2H_4OH + OH$	9.41E + 07	1.70	5459.	[76]
128.	$C_2H_5OH + O = sC_2H_4OH + OH$	1.88E + 07	1.85	1842.	[76]
129.	$C_2H_5OH + CH_3 = pC_2H_4OH + CH_4$	1.33E + 02	3.18	9362.	[76]
130.	$C_2H_5OH + CH_3 = sC_2H_4OH + CH_4$	4.44E + 02	2.90	7690.	[76]
131.	$C_2H_5OH + C_2H_5 = pC_2H_4OH + C_2H_6$	5.00E + 10	0.00	13400.	[66]
132.	$C_2H_5OH + C_2H_5 = sC_2H_4OH + C_2H_6$	5.00E + 10	0.00	10400.	[66]
133.	$C_2H_4 + OH = pC_2H_4OH$	9.93E + 11	0.00	−960.	[77]
134.	$sC_2H_4OH + M = CH_3CHO + H + M$	1.00E + 14	0.00	25000.	[76]
135.	$C_2H_4 + CH_3 = C_2H_3 + CH_4$	6.62E + 00	3.70	9500.	[40]
136.	$CH_3CO(+M) = CH_3 + CO(+M)$	3.00E + 12	0.00	16722.	[38]
	Low pressure limit	1.20E + 15	0.00	12518.	
137.	$CH_3CHO = CH_3 + HCO$	2.61E + 15	0.15	80550.	† [a]
138.	$CH_3CHO + O_2 = CH_3CO + HO_2$	3.01E + 13	0.00	39148.	[42]
139.	$CH_3CHO + OH = CH_3CO + H_2O$	2.00E + 06	1.80	1300.	[78]
140.	$CH_3CHO + H = CH_3CO + H_2$	1.34E + 13	0.00	3300.	[79]
141.	$CH_3CHO + O = CH_3CO + OH$	5.94E + 12	0.00	1868.	† [a]
142.	$CH_3CHO + HO_2 = CH_3CO + H_2O_2$	3.01E + 12	0.00	11925.	[42]
143.	$CH_3CHO + CH_3 = CH_3CO + CH_4$	2.61E + 06	1.78	5910.	† [a]
144.	$C_2H_4 + O_2 = C_2H_3 + HO_2$	4.00E + 13	0.00	58200.	† [c]
145.	$CO + H_2 + M = CH_2O + M$	5.07E + 27	−3.42	84350.	[56]
146.	$C_2H_4 + CH_3O = C_2H_3 + CH_3OH$	1.20E + 11	0.00	6750.	[40]
147.	$CH_3COCH_3 = CH_3CO + CH_3$	1.22E + 23	−1.99	83950.	† [a]
148.	$CH_3COCH_3 + OH = CH_3COCH_2 + H_2O$	1.05E + 10	0.97	1586.	[66]
149.	$CH_3COCH_3 + H = CH_3COCH_2 + H_2$	5.63E + 07	2.00	7700.	[66]
150.	$CH_3COCH_3 + O = CH_3COCH_2 + OH$	1.13E + 14	0.00	7850.	[66]
151.	$CH_3COCH_3 + CH_3 = CH_3COCH_2 + CH_4$	3.96E + 11	0.00	9784.	† [a]
152.	$CH_3COCH_3 + CH_3O = CH_3COCH_2 + CH_3OH$	1.00E + 11	0.00	7000.	[66]
153.	$CH_3COCH_2 = CH_2CO + CH_3$	1.00E + 14	0.00	31000.	[66]
154.	$CH_3COCH_3 + O_2 = CH_3COCH_2 + HO_2$	1.20E + 14	0.00	46000.	[66]
155.	$CH_3COCH_3 + HO_2 = CH_3COCH_2 + H_2O_2$	1.70E + 13	0.00	20460.	[66]
156.	$C_2H_5 + CO = C_2H_5CO$	1.51E + 11	0.00	4810.	[40]
157.	$C_2H_5CHO + H = C_2H_5CO + H_2$	3.98E + 13	0.00	4200.	[66]
158.	$C_2H_5CHO + O = C_2H_5CO + OH$	5.01E + 12	0.00	1790.	[66]
159.	$C_2H_5CHO + OH = C_2H_5CO + H_2O$	9.24E + 06	1.50	−962.	† [e]
160.	$C_2H_5CHO + CH_3 = C_2H_5CO + CH_4$	2.61E + 06	1.78	5911.	† [a]
161.	$C_2H_5CHO + HO_2 = C_2H_5CO + H_2O_2$	1.00E + 12	0.00	11000.	[66]
162.	$C_2H_5CHO + CH_3O = C_2H_5CO + CH_3OH$	1.00E + 12	0.00	3300.	[66]
163.	$C_2H_5CHO + C_2H_5 = C_2H_5CO + C_2H_6$	1.00E + 12	0.00	8000.	[66]
164.	$C_2H_5 + HCO = C_2H_5CHO$	1.81E + 13	0.00	0.	[40]
165.	$C_2H_5CHO + O_2 = C_2H_5CO + HO_2$	2.00E + 13	0.50	42200.	[66]
166.	$C_2H_5CHO + C_2H_3 = C_2H_5CO + C_2H_4$	1.70E + 12	0.00	8440.	[66]
167.	$H_2O_2 + H = H_2 + HO_2$	4.82E + 13	0.00	7950.	[40]

168.	$HCO + O = CO_2 + H$	3.00E + 13	0.00	0.	[39]
169.	$CH_3 + M = CH_2 + H + M$	1.97E + 16	0.00	92520.	† [a]
170.	$CH_3 + H = CH_2 + H_2$	9.00E + 13	0.00	15100.	[68]
171.	$CH_3 + OH = CH_2 + H_2O$	3.00E + 06	2.00	2500.	[38]
172.	$CH + CH_4 = C_2H_4 + H$	6.00E + 13	0.00	0.	[68]
173.	$CH_3OH(+M) = CH_2OH + H(+M)$	2.69E + 16	−0.08	98940.	[49]
	Low pressure limit	2.34E + 40	−6.33	103100.	
	Troe parameters a=0.773,				
	T^{***} = 693., T^{*} = 5333., T^{**} = 1.0E+100.				
	Enhanced Third Body Efficiencies:				
	H_2 = 2.0, H_2O = 5.0, CO = 2.0, CO_2 = 3.0				
174.	$CH_3CO + H = CH_2CO + H_2$	2.00E + 13	0.00	0.	[66]
175.	$CH_3CO + O = CH_2CO + OH$	2.00E + 13	0.00	0.	[66]
176.	$CH_3CO + CH_3 = CH_2CO + CH_4$	5.00E + 13	0.00	0.	[66]
177.	$C_2H_4 + O = CH_2CHO + H$	3.39E + 06	1.88	179.	[61]
178.	$C_2H_5 + O = CH_3CHO + H$	5.00E + 13	0.00	0.	[66]
179.	$C_2H_6 + CH = C_2H_5 + CH_2$	1.10E + 14	0.00	−260.	[42]
180.	$CH_3OH + HCO = CH_2OH + CH_2O$	9.63E + 03	2.90	13110.	[49]
181.	$C_2H_5OH + OH = C_2H_5O + H_2O$	7.46E + 11	0.30	1634.	[76]
182.	$C_2H_5OH + H = C_2H_5O + H_2$	1.50E + 07	1.60	3038.	[76]
183.	$C_2H_5OH + O = C_2H_5O + OH$	1.58E + 07	2.00	4448.	[76]
184.	$C_2H_5OH + CH_3 = C_2H_5O + CH_4$	1.34E + 02	2.92	7452.	[76]
185.	$sC_2H_4OH + O_2 = CH_3CHO + HO_2$	3.81E + 06	2.00	1641.	† [f]
186.	$C_2H_5O + O_2 = CH_3CHO + HO_2$	4.28E + 10	0.00	1097.	[80]
187.	$H_2O_2 + O_2 = HO_2 + HO_2$	1.30E + 11	0.00	−1629.	[63]
188.	$H_2O_2 + OH = H_2O + HO_2$	5.80E + 14	0.00	9560.	[48]
189.	$C_2H_5O_2 = C_2H_5 + O_2$	4.93E + 50	−11.50	42250.	[51]
190.	$CH_3 + O_2 + M = CH_3O_2 + M$	5.44E + 25	−3.30	0.	[42]
191.	$CH_3O_2H = CH_3O + OH$	6.31E + 14	0.00	42300.	[81]
192.	$C_2H_5O_2H = C_2H_5O + OH$	6.31E + 14	0.00	42300.	† [g]
193.	$C_2H_5O + M = CH_3 + CH_2O + M$	1.35E + 38	−6.96	23800.	[76]
194.	$CH_3O_2 + CH_2O = CH_3O_2H + HCO$	1.99E + 12	0.00	11670.	[40]
195.	$C_2H_5O_2 + CH_2O = C_2H_5O_2H + HCO$	1.99E + 12	0.00	11670.	† [h]
196.	$C_2H_4 + CH_3O_2 = C_2H_3 + CH_3O_2H$	1.13E + 13	0.00	30430.	[66]
197.	$C_2H_4 + C_2H_5O_2 = C_2H_3 + C_2H_5O_2H$	1.13E + 13	0.00	30430.	[66]
198.	$CH_4 + CH_3O_2 = CH_3 + CH_3O_2H$	1.81E + 11	0.00	18480.	[40]
199.	$CH_4 + C_2H_5O_2 = CH_3 + C_2H_5O_2H$	1.81E + 11	0.00	18480.	† [h]
200.	$CH_3OH + CH_3O_2 = CH_2OH + CH_3O_2H$	1.81E + 12	0.00	13710.	[71]
201.	$CH_3OH + C_2H_5O_2 = CH_2OH + C_2H_5O_2H$	1.81E + 12	0.00	13710.	† [h]
202.	$C_2H_5 + HO_2 = C_2H_5O + OH$	3.20E + 13	0.00	0.	[51]
203.	$CH_3O_2 + CH_3 = CH_3O + CH_3O$	7.00E + 12	0.00	−1000.	† [i]
204.	$CH_3O_2 + C_2H_5 = CH_3O + C_2H_5O$	7.00E + 12	0.00	−1000.	† [i]
205.	$CH_3O_2 + HO_2 = CH_3O_2H + O_2$	1.75E + 10	0.00	−3275.	† [j]

206.	$CH_3OH + O_2 = CH_2OH + HO_2$	2.05E + 13	0.00	44900.	[71]
207.	$C_2H_5O_2 + HO_2 = C_2H_5O_2H + O_2$	1.75E + 10	0.00	−3275.	† [j]
208.	$CH_3O_2 + CH_3O_2 = CH_2O + CH_3OH + O_2$	3.11E + 14	−1.61	−1051.	[82]
209.	$CH_3O_2 + CH_3O_2 = O_2 + CH_3O + CH_3O$	1.40E + 16	−1.61	1860.	[82]
210.	$C_2H_6 + CH_3O_2 = C_2H_5 + CH_3O_2H$	1.70E + 13	0.00	20460.	† [k]
211.	$C_2H_6 + C_2H_5O_2 = C_2H_5 + C_2H_5O_2H$	1.70E + 13	0.00	20460.	† [k]
212.	$pC_2H_4OH + O_2 = O_2C_2H_4OH$	1.20E + 11	0.00	−1100.	† [l]
213.	$O_2C_2H_4OH = OH + CH_2O + CH_2O$	1.25E + 10	0.00	18900.	† [m]
214.	$C_2H_5O_2 = C_2H_4O_2H$	5.64E + 47	−11.44	37320.	[51]
215.	$C_2H_4O_2H = C_2H_4O1\text{-}2 + OH$	4.25E + 22	−4.18	22350.	[51]
216.	$CH_3CO + O_2 = CH_3CO_3$	1.20E + 11	0.00	−1100.	† [l]
217.	$CH_3CO_2 + M = CH_3 + CO_2 + M$	4.40E + 15	0.00	10500.	[66]
218.	$CH_3CO_3H = CH_3CO_2 + OH$	5.01E + 14	0.00	40150.	[83]
219.	$CH_3CO_3 + HO_2 = CH_3CO_3H + O_2$	1.75E + 10	0.00	−3275.	† [j]
220.	$C_2H_5O + M = CH_3CHO + M$	1.16E + 35	−5.89	25274.	[76]
221.	$H_2O_2 + CH_3CO_3 = HO_2 + CH_3CO_3H$	2.40E + 12	0.00	9936.	† [h]
222.	$CH_4 + CH_3CO_3 = CH_3 + CH_3CO_3H$	1.81E + 11	0.00	18480.	† [h]
223.	$C_2H_4 + CH_3CO_3 = C_2H_3 + CH_3CO_3H$	1.13E + 13	0.00	30430.	[66]
224.	$C_2H_6 + CH_3CO_3 = C_2H_5 + CH_3CO_3H$	1.70E + 13	0.00	20460.	† [k]
225.	$CH_2O + CH_3CO_3 = HCO + CH_3CO_3H$	1.99E + 12	0.00	11670.	† [h]
226.	$CH_3O_2 + CH_3CHO = CH_3O_2H + CH_3CO$	3.01E + 12	0.00	11925.	† [e]
227.	$CH_3CHO + CH_3CO_3 = CH_3CO + CH_3CO_3H$	3.01E + 12	0.00	11925.	† [e]
228.	$C_2H_3 + CO = C_2H_3CO$	1.51E + 11	0.00	4810.	[40]
229.	$C_2H_3CHO + OH = C_2H_3CO + H_2O$	9.24E + 06	1.50	−962.	† [e]
230.	$C_2H_3CHO + H = C_2H_3CO + H_2$	1.34E + 13	0.00	3300.	† [e]
231.	$C_2H_3CHO + O = C_2H_3CO + OH$	5.94E + 12	0.00	1868.	† [e]
232.	$C_2H_3CHO + HO_2 = C_2H_3CO + H_2O_2$	3.01E + 12	0.00	11925.	† [e]
233.	$C_2H_3CHO + CH_3 = C_2H_3CO + CH_4$	2.61E + 06	1.78	5910.	† [e]
234.	$C_2H_3CHO + CH_3O_2 = C_2H_3CO + CH_3O_2H$	3.01E + 12	0.00	11925.	† [e]
235.	$C_2H_4O_2H = C_2H_4 + HO_2$	9.29E + 30	−6.10	19930.	[51]
236.	$C_2H_4 + CH_3O_2 = C_2H_4O1\text{-}2 + CH_3O$	2.82E + 12	0.00	17110.	† [n]
237.	$C_2H_4 + C_2H_5O_2 = C_2H_4O1\text{-}2 + C_2H_5O$	2.82E + 12	0.00	17110.	† [n]
238.	$C_2H_4O1\text{-}2 = CH_3 + HCO$	3.63E + 13	0.00	57200.	[84]
239.	$C_2H_4O1\text{-}2 = CH_3CHO$	7.41E + 12	0.00	53800.	† [a]
240.	$C_2H_4O1\text{-}2 + OH = C_2H_3O1\text{-}2 + H_2O$	1.78E + 13	0.00	3610.	[85]
241.	$C_2H_4O1\text{-}2 + H = C_2H_3O1\text{-}2 + H_2$	8.00E + 13	0.00	9600.	[85]
242.	$C_2H_4O1\text{-}2 + HO_2 = C_2H_3O1\text{-}2 + H_2O_2$	1.13E + 13	0.00	30430.	[66]
243.	$C_2H_4O1\text{-}2 + CH_3O_2 = C_2H_3O1\text{-}2 + CH_3O_2H$	1.13E + 13	0.00	30430.	[66]
244.	$C_2H_4O1\text{-}2 + C_2H_5O_2 = C_2H_3O1\text{-}2 + C_2H_5O_2H$	1.13E + 13	0.00	30430.	[66]
245.	$C_2H_4O1\text{-}2 + CH_3 = C_2H_3O1\text{-}2 + CH_4$	1.07E + 12	0.00	11830.	[85]
246.	$C_2H_4O1\text{-}2 + CH_3O = C_2H_3O1\text{-}2 + CH_3OH$	1.20E + 11	0.00	6750.	[66]
247.	$CH_3COCH_2 + O_2 = CH_3COCH_2O_2$	1.20E + 11	0.00	−1100.	† [l]
248.	$CH_3COCH_3 + RO_2 = CH_3COCH_2 + CH_3COCH_2O_2H$	1.00E + 11	0.00	5000.	[66]

249.	$CH_2O + CH_3COCH_2O_2 = HCO + CH_3COCH_2O_2H$	1.29E + 11	0.00	9000.	[66]
250.	$HO_2 + CH_3COCH_2O_2 = CH_3COCH_2O_2H + O_2$	1.00E + 12	0.00	0.	[66]
251.	$CH_3COCH_2O_2H = CH_3COCH_2O + OH$	1.00E + 16	0.00	43000.	† [o]
252.	$CH_3CO + CH_2O = CH_3COCH_2O$	1.00E + 11	0.00	11900.	† [p]
253.	$C_2H_5CHO + CH_3O_2 = C_2H_5CO + CH_3O_2H$	3.01E + 12	0.00	11930.	† [e]
254.	$C_2H_5CHO + C_2H_5O = C_2H_5CO + C_2H_5OH$	6.03E + 11	0.00	3300.	[66]
255.	$C_2H_5CHO + C_2H_5O_2 = C_2H_5CO + C_2H_5O_2H$	3.01E + 12	0.00	11930.	† [e]
256.	$C_2H_5CHO + CH_3CO_3 = C_2H_5CO + CH_3CO_3H$	3.01E + 12	0.00	11930.	† [e]
257.	$CH_3CHO + OH = CH_3 + HOCHO$	3.00E + 15	−1.08	0.	[78]
258.	$C_2H_3O1\text{-}2 = CH_3CO$	8.50E + 14	0.00	14000.	[66]
259.	$C_2H_3O1\text{-}2 = CH_2CHO$	1.00E + 14	0.00	14000.	[66]
260.	$CH_2CHO = CH_2CO + H$	3.09E + 15	−0.26	50820.	† [p]
261.	$CH_2CHO + O_2 = CH_2O + CO + OH$	2.00E + 13	0.00	4200.	† [p]
262.	$HCO + O_2 = O_2CHO$	1.20E + 11	0.00	−1100.	† [l]
263.	$CH_2O + O_2CHO = HCO + HO_2CHO$	1.99E + 12	0.00	11670.	† [k]
264.	$HO_2CHO = OCHO + OH$	5.01E + 14	0.00	40150.	† [o]
265.	$H + CO_2 + M = OCHO + M$	7.50E + 13	0.00	29000.	† [p]
266.	$HCCO + O_2 = CO_2 + HCO$	2.40E + 11	0.00	−854.	[76]
267.	$CH_3CHO + OH = CH_2CHO + H_2O$	1.72E + 05	2.40	815.	[78]
268.	$CH_2CO + OH = CH_2OH + CO$	3.73E + 12	0.00	−1013.	[86]
269.	$CH_3 + O_2 = CH_2O + OH$	7.47E + 11	0.00	14250.	[87]
270.	$CH_3 + CH_3 = C_2H_4 + H_2$	1.00E + 14	0.00	32000.	[88]
271.	$CH_3 + OH = CH_2[s] + H_2O$	2.65E + 13	0.00	2186.	[57]
272.	$C_2H_4 + HO_2 = C_2H_4O1\text{-}2 + OH$	2.23E + 12	0.00	17190.	[42]
273.	$CH_3OCH_3 = CH_3 + CH_3O$	1.90E + 68	−15.27	108939.	† [q]
274.	$CH_3OCH_3 + OH = CH_3OCH_2 + H_2O$	9.35E + 05	2.29	−780.7	†
275.	$CH_3OCH_3 + H = CH_3OCH_2 + H_2$	7.72E + 06	2.09	3384.	† [a]
276.	$CH_3OCH_3 + O = CH_3OCH_2 + OH$	1.86E − 03	5.29	−109.	[11]
277.	$CH_3OCH_3 + HO_2 = CH_3OCH_2 + H_2O_2$	1.68E + 13	0.00	17690.	[11]
278.	$CH_3OCH_3 + CH_3O_2 = CH_3OCH_2 + CH_3O_2H$	1.68E + 13	0.00	17690.	[11]
279.	$CH_3OCH_3 + CH_3 = CH_3OCH_2 + CH_4$	1.45E − 06	5.73	5699.	† [a]
280.	$CH_3OCH_3 + O_2 = CH_3OCH_2 + HO_2$	4.10E + 13	0.00	44910.	[11]
281.	$CH_3OCH_3 + CH_3O = CH_3OCH_2 + CH_3OH$	6.02E + 11	0.00	4074.	† [r]
282.	$CH_3OCH_2 = CH_2O + CH_3$	1.60E + 13	0.00	25500.	[89]
283.	$CH_3OCH_2 + CH_3O = CH_3OCH_3 + CH_2O$	2.41E + 13	0.00	0.	[11]
284.	$CH_3OCH_2 + CH_2O = CH_3OCH_3 + HCO$	5.49E + 03	2.80	5862.	[11]
285.	$CH_3OCH_2 + CH_3CHO = CH_3OCH_3 + CH_3CO$	1.26E + 12	0.00	8499.	[11]
286.	$CH_3OCH_2 + HO_2 = CH_3OCH_2O + OH$	9.00E + 12	0.00	0.	[11]
287.	$CH_3OCH_2 + O_2 = CH_3OCH_2O_2$	2.00E + 12	0.00	0.	[11]
288.	$CH_3OCH_3 + R'O_2 = CH_3OCH_2 + CH_3OCH_2O_2H$	5.00E + 12	0.00	17690.	† [k]
289.	$CH_3OCH_2O_2 + CH_2O = CH_3OCH_2O_2H + HCO$	1.00E + 12	0.00	11670.	† [h]
290.	$R'O_2 + CH_3CHO = CH_3OCH_2O_2H + CH_3CO$	2.80E + 12	0.00	13600.	[11]
291.	$CH_3OCH_2O + OH = CH_3OCH_2O_2H$	2.00E + 13	0.00	0.	[11]

292.	$CH_3O + CH_2O = CH_3OCH_2O$	1.00E + 11	0.00	11900.	† [p]
293.	$CH_3OCH_2O_2 = CH_2OCH_2O_2H$	6.00E + 10	0.00	21580.	[15]
294.	$CH_2OCH_2O_2H = OH + CH_2O + CH_2O$	1.50E + 13	0.00	20760.	[15]
295.	$CH_2OCH_2O_2H + O_2 = O_2CH_2OCH_2O_2H$	7.00E + 11	0.00	0.	[15]
296.	$O_2CH_2OCH_2O_2H = HO_2CH_2OCHO + OH$	4.00E + 10	0.00	18580.	[15]
297.	$HO_2CH_2OCHO = OCH_2OCHO + OH$	2.00E + 16	0.00	40500.	[15]
298.	$CH_2O + OCHO = OCH_2OCHO$	1.25E + 11	0.00	11900.	[15]
299.	$C_2H_5O_2 = C_2H_4 + HO_2$	3.37E + 55	−13.42	44670.	[51]
300.	$C_2H_4O_2H = C_2H_5 + O_2$	2.15E + 37	−8.21	28020.	[51]
301.	$CH_3O + CH_3 = CH_2O + CH_4$	2.40E + 13	0.00	0.	[40]
302.	$CH_3OCH_3 + O_2CHO = CH_3OCH_2 + HO_2CHO$	4.42E + 04	2.60	13910.	† [h]
303.	$OCH_2OCHO = HOCH_2OCO$	1.00E + 11	0.00	14000.	[15]
304.	$HOCH_2O + CO = HOCH_2OCO$	1.50E + 11	0.00	4800.	[15]
305.	$CH_2OH + CO_2 = HOCH_2OCO$	1.50E + 11	0.00	35200.	[15]
306.	$CH_2OH + HO_2 = HOCH_2O + OH$	1.00E + 13	0.00	0.	† [s]
307.	$CH_2O + OH = HOCH_2O$	4.50E + 15	−1.10	0.	[15]
308.	$HOCH_2O = HOCHO + H$	1.00E + 14	0.00	14900.	[90]
309.	$HOCHO + M = CO + H_2O + M$	2.30E + 13	0.00	50000.	[91]
310.	$HOCHO + M = CO_2 + H_2 + M$	1.50E + 16	0.00	57000.	[91]
311.	$R'O_2 + R'O_2 = CH_3OCHO + CH_3OCH_2OH + O_2$	6.63E + 22	−4.50	0.	[92, 93]
312.	$R'O_2 + R'O_2 = O_2 + CH_3OCH_2O + CH_3OCH_2O$	1.55E + 23	−4.50	0.	[92, 93]
313.	$CH_3OCH_2O = CH_3OCHO + H$	1.75E + 16	−0.66	11720.	† [p]
314.	$CH_3OCHO = CH_3 + OCHO$	1.39E + 18	−0.99	79140.	† [p]
315.	$CH_3OCHO + O_2 = CH_3OCO + HO_2$	1.00E + 13	0.00	49700.	† [c]
316.	$CH_3OCHO + OH = CH_3OCO + H_2O$	2.34E + 07	1.61	−35.	† [p]
317.	$CH_3OCHO + HO_2 = CH_3OCO + H_2O_2$	1.22E + 12	0.00	17000.	† [p]
318.	$CH_3OCHO + O = CH_3OCO + OH$	2.35E + 05	2.50	2230.	† [p]
319.	$CH_3OCHO + H = CH_3OCO + H_2$	4.55E + 06	2.00	5000.	† [p]
320.	$CH_3OCHO + CH_3 = CH_3OCO + CH_4$	7.55E − 01	3.46	5481.	† [p]
321.	$CH_3OCHO + CH_3O = CH_3OCO + CH_3OH$	5.48E + 11	0.00	5000.	† [p]
322.	$CH_3OCHO + CH_3O_2 = CH_3OCO + CH_3O_2H$	1.22E + 12	0.00	17000.	† [p]
323.	$CH_3O + CO = CH_3OCO$	1.50E + 11	0.00	3000.	† [p]
324.	$CH_3 + CO_2 = CH_3OCO$	1.50E + 11	0.00	36730.	† [p]
325.	$CH_2O + HO_2 = OCH_2O_2H$	1.50E + 11	0.00	11900.	† [p]
326.	$OCH_2O_2H = HOCH_2O_2$	3.00E + 11	0.00	8600.	† [p]
327.	$HOCH_2O_2 + HO_2 = HOCH_2O_2H + O_2$	3.50E + 10	0.00	−3275.	† [j]
328.	$CH_3OCH_3 + OCHO = CH_3OCH_2 + HOCHO$	1.00E + 13	0.00	17690.	† [d]
329.	$HCO + OH = HOCHO$	1.00E + 14	0.00	0.	† [p]
330.	$CH_2O + OCHO = HCO + HOCHO$	5.60E + 12	0.00	13600.	† [j]
331.	$OCHO + HO_2 = HOCHO + O_2$	3.50E + 10	0.00	−3275.	† [k]
332.	$OCHO + H_2O_2 = HOCHO + HO_2$	2.40E + 12	0.00	10000.	† [p]
333.	$HOCHO + OH = H_2O + CO_2 + H$	2.62E + 06	2.06	916.	[76]
334.	$HOCHO + OH = H_2O + CO + OH$	1.85E + 07	1.51	−962.	[76]

335.	$HOCHO + H = H_2 + CO_2 + H$	4.24E + 06	2.10	4868.	[76]
336.	$HOCHO + H = H_2 + CO + OH$	6.03E + 13	−0.35	2988.	[76]
337.	$HOCHO + CH_3 = CH_4 + CO + OH$	3.90E − 07	5.80	2200.	[76]
338.	$HOCHO + HO_2 = H_2O_2 + CO + OH$	1.00E + 12	0.00	11920.	[76]
339.	$HOCHO + O = CO + OH + OH$	1.77E + 18	−1.90	2975.	[76]
340.	$CH_2[s] + M = CH_2 + M$	1.00E + 13	0.00	0.	[68]
341.	$CH_2[s] + CH_4 = CH_3 + CH_3$	4.00E + 13	0.00	0.	[68]
342.	$CH_2[s] + C_2H_6 = CH_3 + C_2H_5$	1.20E + 14	0.00	0.	[68]
343.	$CH_2[s] + O_2 = CO + OH + H$	7.00E + 13	0.00	0.	[68]
344.	$CH_2[s] + H_2 = CH_3 + H$	7.00E + 13	0.00	0.	[68]
345.	$CH_2[s] + H = CH + H_2$	3.00E + 13	0.00	0.	[68]
346.	$CH_2[s] + O = CO + H + H$	3.00E + 13	0.00	0.	[68]
347.	$CH_2[s] + OH = CH_2O + H$	3.00E + 13	0.00	0.	[68]
348.	$CH_2[s] + CO_2 = CH_2O + CO$	3.00E + 12	0.00	0.	[68]
349.	$CH_2[s] + CH_3 = C_2H_4 + H$	2.00E + 13	0.00	0.	[68]
350.	$CH_2[s] + CH_2CO = C_2H_4 + CO$	1.60E + 14	0.00	0.	[68]
351.	$C_2H_3 + O_2 = CH_2CHO + O$	3.50E + 14	−0.61	5260.	[38]

Table 1: Dimethyl Ether Mechanism Rate Coefficients; cm^3/mol/sec/cal units. †: *this study, see footnote.* $RO_2 = CH_3COCH_2O_2$, $R'O_2 = CH_3OCH_2O_2$.

a: NIST fit [95] to experimental data.
b: NIST fit [95] to recommendation of Baulch et al. [42] and Irdam et al. [96].
c: Walker [97] recommendation for RH + O_2 reaction.
d: Walker [98] recommendation for RH + $H\dot{O}_2$ reaction.
e: Based on $CH_3CHO + \dot{R} = CH_3CO + RH$.
f: Based on $CH_2OH + O_2 = CH_2O + HO_2$.
g: Based on CH_3O_2H decomposition.
h: Based on $CH_3O_2 + RH = CH_3O_2H + R$.
i: Rate expression employed for $R + RO_2 = RO + RO$ in our kinetic models.
j: Rate expression employed for $RO_2 + HO_2 = RO_2H + O_2$ in our kinetic models.
k: Based on $RH + HO_2 = R + H_2O_2$.
l: Based on NIST fit to $C_2H_5 + O_2 = C_2H_5O_2$.
m: Based on our estimates for $RO_2 \rightleftharpoons$ QOOH isomerization reactions.
n: Based on $C_2H_4 + HO_2$.
o: Based on typical $RO_2H = RO + OH$ recommended by Sahetchian et al. [83].
p: Curran estimate.
q: Rate expression calculated at 1 atm using QRRK theory [99, 100].
r: By analogy with $C_3H_8 + CH_3O$.
s: Rate expression employed for $R + HO_2 = RO + OH$ in our kinetic models.

Discussion

The primary products formed during both high temperature pyrolysis and oxidation are carbon monoxide (CO), carbon dioxide (CO_2), formaldehyde (CH_2O), methane (CH_4), ethane (C_2H_6) and ethylene (C_2H_4). In addition, water (H_2O), which is not observed during pyrolysis is a product of oxidation. Comparisons of the product species profiles measured in

the experiment and predicted in the model simulation are shown in Figs. 7–10 for the two pyrolysis mixtures, and in Figs. 11–16 for the oxidation experiments. The model-predicted concentration profiles for each product species are in very good agreement with the experimental results for almost all conditions. The main discrepancy is in the measured and predicted methane profiles at fuel-lean conditions, Fig. 12. The measured methane profile is about a factor of three greater than that predicted by the model. We do not, as yet, have a satisfactory explanation for why this is so. Product formation can be fully explained by the reaction scheme discussed below.

Dimethyl Ether Pyrolysis

During pyrolysis, initiation occurs *via* unimolecular decomposition:

$$CH_3OCH_3 \xrightarrow{273} CH_3\dot{O} + \dot{C}H_3$$

The rate constant for the unimolecular decomposition of DME was estimated using a chemical activation formulation based on Quantum Rice-Ramsperger-Kassel (QRRK) theory, as described by Dean [99, 100]. This analysis uses a high pressure limit rate constant of 1.24×10^{15} $T^{0.32}$ exp(-39780/T) s^{-1}. This rate constant was calculated from microscopic reversibility by using a rate expression of 3.0×10^{13} cm^3 mol^{-1} s^{-1} for $CH_3\dot{O} + \dot{C}H_3$ addition. We estimate the rate expression in the reverse direction, as typically the addition of two radical species has no associated activation energy and the A-factor is normally between 2–3 $\times 10^{13}$. For example, for the reaction $\dot{C}_2H_5 + \dot{C}H_3 = C_3H_8$, Baulch et al. [42, 61] recommend rates of 2.83–3.37 $\times 10^{13}$. In a previous study [11] we used 2.75×10^{13} cm^3 mol^{-1} s^{-1} as the high-pressure limit for reaction (-273). (The earlier paper erroneously reported this rate as 5.0×10^{13} cm^3 mol^{-1} s^{-1}). The current rate constant expression at a pressure of 1 atm is provided in Table 1, and is almost a factor of two faster than the previously published value. Figure 17 depicts our recommended rate expression for the unimolecular decomposition, calculated at 1 atm using QRRK theory, our previously published rate expression at 1 atm and the literature values of Pacey [101] measured at 25–395 Torr, Aronowitz and Naegeli [102] measured at 1 atm, and Batt et al. [103] measured in the pressure range 400–800 Torr. Our current recommendation at 1 atm is almost identical to that measured by Aronowitz and Naegeli and is in very good agreement with the measurement of Pacey.

The methoxy radical formed in reaction (273) undergoes β-scission to yield formaldehyde and a hydrogen atom, reaction (40). The hydrogen atom formed in reaction (40) and the methyl radical formed in reaction (273) abstract a hydrogen atom from the fuel to form the methoxymethyl radical, reactions (275) and (279). The methoxymethyl radical then undergoes β-scission to yield formaldehyde and a methyl radical, reaction (282), and, as the radical pool becomes more established, this is the predominant route to formaldehyde formation. Our rate expression for the β-scission of the methoxymethyl radical is that measured by Loucks and Laidler [89].

$$CH_3\dot{O} \xrightarrow{40} CH_2O + \dot{H}$$

$$CH_3OCH_3 + \dot{H} \xrightarrow{275} CH_3O\dot{C}H_2 + H_2$$

$$CH_3OCH_3 + \dot{C}H_3 \xrightarrow{279} CH_3O\dot{C}H_2 + CH_4$$

$$CH_3O\dot{C}H_2 \xrightarrow{282} CH_2O + \dot{C}H_3$$

It is not surprising to find that the overall rate of pyrolysis is very dependent on the rates of these reactions. The rate expression for reaction (275) was estimated using a NIST database fit [95] to the experimental measurements of Meagher et al. [104], Faubel et al. [105] and Lee et al. [106] and using the estimation of Aronowitz and Naegeli. A comparison of our rate expression with those available in the literature is plotted in Fig. 18.

The rate of abstraction of a hydrogen atom from DME by a methyl radical, reaction (279), was also estimated using a NIST database fit. We used the experimental data of Batt et al. [103], Pacey [101], Arthur et al. [107] and Gray and Herod [108]. A comparison of our rate expression with those available in the literature is plotted in Fig. 19.

Figure 30 shows the sensitivity under near-pyrolysis conditions, and indicates the importance of H-atom abstraction reactions from fuel and formaldehyde by hydrogen atoms and methyl radicals. Figures 21–compr4 indicate that there is very good correlation in the rate expressions for DME + $\dot{C}H_3$, reaction (279), and CH_2O + $\dot{C}H_3$, reaction (38). The greatest relative errors lie in the rate constant expressions for DME + $\dot{H}$, reaction (275), and CH_2O + $\dot{H}$, reaction (33). However, the more recent rate expressions [56] and [129, 130] for reaction (33) are in good agreement with one another, and our chosen rate expression is approximately 30% lower than these. Thus, we feel our rate expression for reaction (275), fitted to the current data, and developed using the "best fit" to the current mechanism is quite reliable.

The concentration of formaldehyde produced in our simulation is dependent on the relative rates of abstraction by hydrogen atom and methyl radical from dimethyl ether and formaldehyde. Figure 20 depicts the predicted formaldehyde concentration profile versus time by changing the rates of the unimolecular and abstraction reactions by a factor of two. An increase in the rates of abstraction from DME increases the concentration of formaldehyde while an increase in the rate of abstraction from formaldehyde lowers its observed concentration. We estimated the rate of hydrogen atom abstraction from formaldehyde by a $\dot{H}$ atom, reaction (33), using a NIST database fit [95] to the recommendation of Baulch et al. [42] and Irdam et al. [96]. The rate expression for H atom abstraction by a $\dot{C}H_3$ radical, reaction (38), is based on a NIST fit to the recommendations of Manthorne and Pacey [109], Choudhury et al. [110, 111] and on the experimental data of Anastasi [112]. The rate constant expression for reaction (33) is compared to other literature recommendations in Fig. 21 which includes the most recent recommendations of Eiteneer et al. [56]. Similarly, our rate expressions for reaction (38) is compared with literature values in Fig. 22.

Dimethyl Ether Oxidation

Dimethyl ether consumption characteristics for oxidative conditions are similar to those observed in the pyrolysis experiments. Initiation occurs *via* unimolecular fuel decomposition. The contribution of hydrogen atom abstraction from the fuel by molecular oxygen, reaction (280) is minimal, with $\leq 1.0\%$ contributing to initiation, even under fuel-lean conditions. Once the radical pool becomes established, hydrogen atom abstraction from the fuel by $\dot{H}$ atoms, reaction (275), and $\dot{C}H_3$ radicals, reaction (279), becomes as important as unimolecular decomposition, reaction (273), with the rates of all three reactions achieving values within a factor of two of one another.

The main difference between oxidation and pyrolysis is in the contribution of $\dot{O}H$ radical attack on the fuel, reaction (274). As a result, water is noted and quantified in the oxidation

experiments, while it was not observed during pyrolysis. Our recommended rate expression for reaction (274) is taken from a NIST database fit [116] to the experimental data of Arif et al. [117], Mellouki et al. [118], Nelson et al. [119], Wallington et al. [120], Tully and Droege [121] and the previously recommended rate expression [11]. The rate of reaction (274) is similar to that observed for reactions (275), (279) and (273). For example, under stoichiometric conditions, Figs. 13 and 14, and at 20% fuel conversion, the rates of reactions (275), (279), (274) and (273) are 1.01×10^{-7}, 9.62×10^{-8}, 8.93×10^{-8} and 5.10×10^{-8} mol cm^{-3} s^{-1}, respectively. Under fuel-lean conditions, reaction (274) becomes more important as there is a higher concentration of hydroxyl radicals than under fuel-rich conditions. Hydroxyl radicals are produced *via* four main pathways, all of which are dependent, either directly or indirectly, on the concentration of molecular oxygen:

$$\begin{aligned}
CH_3OCH_3 + \dot{O}H &\xrightarrow{274} CH_3O\dot{C}H_2 + H_2O \\
\dot{C}H_3 + H\dot{O}_2 &\xrightarrow{22} CH_3\dot{O} + \dot{O}H \\
\dot{C}H_3 + O_2 &\xrightarrow{269} CH_2O + \dot{O}H \\
\dot{H} + O_2 &\xrightarrow{8} \dot{O} + \dot{O}H \\
CH_3OCH_3 + \dot{O} &\xrightarrow{276} CH_3O\dot{C}H_2 + \dot{O}H \\
H\dot{C}O + O_2 &\xrightarrow{46} CO + H\dot{O}_2 \\
\dot{H} + O_2 &\xrightarrow{-26} H\dot{O}_2
\end{aligned}$$

Under fuel-lean conditions and at 20% fuel consumption, the relative rates of reactions (22), (269), (8) and (276) are 2.3:1.3:1.0:1.0, respectively. At these conditions, about 90% of the $H\dot{O}_2$ radical is produced *via* reaction (46) above, with the remainder being produced *via* reaction (26).

Methyl radicals, which are formed by unimolecular fuel decomposition, reaction (273), and by methoxymethyl radical β-scission, reaction (282), react with formaldehyde, molecular hydrogen, DME, and $H\dot{O}_2$ to yield methane and a radical species.

$$\begin{aligned}
CH_2O + \dot{C}H_3 &\xrightarrow{38} H\dot{C}O + CH_4 \\
\dot{C}H_3 + H_2 &\xrightarrow{-2} CH_4 + \dot{H} \\
\dot{C}H_3 + H\dot{O}_2 &\xrightarrow{45} CH_4 + O_2
\end{aligned}$$

Hydrogen atoms are generated from the decomposition of both formyl radical, reaction (12), and methoxy radical, reaction (40) above. Reaction (12) also leads to the formation of carbon monoxide which reacts with $H\dot{O}_2$ radical and to a lesser extent with $\dot{O}H$ radical to form carbon dioxide and a $\dot{O}H$ radical and a $\dot{H}$ atom, respectively.

$$\begin{aligned}
H\dot{C}O &\xrightarrow{12} \dot{H} + CO \\
CO + H\dot{O}_2 &\xrightarrow{23} CO_2 + \dot{O}H \\
CO + \dot{O}H &\xrightarrow{7} CO_2 + \dot{H}
\end{aligned}$$

Under fuel-lean conditions, less H_2, CH_4 and CO and more CO_2 are produced relative to the stoichiometric case. This is because the higher absolute concentration of O_2 in this experiment results in the production of greater quantities of $H\dot{O}_2$ radical. This radical reacts with methyl radicals forming $CH_3\dot{O}$ and $\dot{O}H$ radicals, reaction (22) above. The methoxy radical decomposes to formaldehyde which subsequently yields CO which is oxidized to CO_2. Under fuel-rich conditions the reverse is true, higher concentrations of H_2 and CH_4 are formed due to the reduced concentration of $H\dot{O}_2$ radicals.

The formation of ethane is explained by the recombination of methyl radicals, reaction (24). The rate constant expression for this reaction was taken from the work of Walter et al. [125] which includes a Troe fall-off fit.

$$C_2H_6 + (M) \xrightarrow{24} \dot{C}H_3 + \dot{C}H_3 + (M)$$

Ethane subsequently undergoes hydrogen atom abstraction by $\dot{H}$, $\dot{O}H$ and $\dot{C}H_3$ radicals, forming ethyl radical, $\dot{C}_2H_5$, which decomposes to ethene and a hydrogen atom.

$$C_2H_6 + \dot{R} \longrightarrow \dot{C}_2H_5 + RH$$

$$\dot{C}_2H_5 + M \xrightarrow{15} C_2H_4 + \dot{H} + M$$

Comparative Flow Reactor Results

The experimental results reported by Alzueta et al. [13] were also compared with calculations using the current kinetic mechanism. Comparison of these experimental profiles with computational modeling results, Fig. 28, requires that both the chemical induction and post-chemical induction phenomena to be modeled, i.e., reaction residence time requires the assignment of a "zero" reaction time. Thus, these comparisons embody the effects of experimental uncertainties associated with impurities and mixing on the induction chemistry. Our current mechanism predicts DME consumption to begin about twenty degrees lower than that observed in the experiments, Fig. 28, although the shapes of the curves are quite similar. Agreement is certainly within the quoted uncertainties of these experiments.

Shock Tube Comparison

The chemical kinetic mechanism was also used to simulate the experimental shock tube results of Simmie et al. [12]. A comparison of the predicted peak [CO] × [O] with the experimentally observed ignition delay times (based on light emission from the reaction of CO with O atoms) are shown in Fig. 29. Good agreement between simulation and experiment is achieved for all equivalence ratios, although predicted values are somewhat too large at lower temperatures. (Similar behavior was observed in earlier modeling the ignition of allene and propyne [126]). Both predicted and experimental ignition delay times decrease with leaner conditions.

Jet-Stirred Reactor Results

Previously published JSR experimental results [9] test the validity of the reaction mechanism in an alternative experimental device and complement the temperature range explored in the current flow reactor study. Comparisons of the product species profiles measured in the experiment and predicted by the model simulation are shown in Figs. 23-27 for a stoichiometric mixture at 1 and 10 atm.

It is clear that the model-predicted concentration profiles for each product species are in good agreement with the experimental results. At 10 atm and in the temperature range 800–875 K, the model predicts more reactivity than observed in the experiments, but at higher temperatures, model and experimental agreement substantially improves.

Sensitivity Analysis

The chemistry edits produced as output from the HCT code provide detailed information on the most important reactions associated with the production and consumption of each species in the kinetic mechanism. By analyzing these edits, it is possible to develop a flux diagram of the major oxidation pathways responsible for DME pyrolysis and oxidation. A detailed sensitivity analysis was performed, by multiplying the rate constant of a reaction by a factor of two (both forward and reverse rate constants). The sensitivity coefficient has been defined as the percentage change in the time taken for a defined percentage of fuel to be consumed. In the near-pyrolysis experiment at 1 atm, Figs. 9 and 10 we performed analyses at 25% and 70% fuel consumption in order to observe sensitivity to initiation and to propagation reactions. Sensitivity to dimethyl ether oxidation was performed under stoichiometric ($\phi = 1.09$) conditions, with analyses performed at time for 25% and 90% fuel consumption. A negative percent change in time indicates an increase in overall reaction rate, while a positive change indicates a decrease in the overall reactivity of the system.

In both the pyrolysis and oxidation studies, the reaction which shows the largest negative sensitivity coefficient, and thus is greatest in promoting the overall reactivity, is reaction (273), the unimolecular decomposition of the fuel. This reaction leads to the initiation of the radical pool, producing a reactive methoxy radical and a methyl radical. H-atom abstraction from the fuel by methyl radicals, reaction (279), shows the next largest negative sensitivity coefficient under both near-pyrolysis and oxidation conditions. This reaction leads to the formation of a methoxymethyl radical, which can decompose to generate formaldehyde and a methyl radical. Another reaction that shows a high negative sensitivity coefficient is the reaction of formaldehyde with methyl radicals, reaction (38).

$$\mathrm{CH_3OCH_3} \xrightarrow{273} \mathrm{CH_3\dot{O} + \dot{C}H_3}$$

$$\mathrm{CH_3OCH_3 + \dot{C}H_3} \xrightarrow{279} \mathrm{CH_3O\dot{C}H_2 + CH_4}$$

$$\mathrm{CH_2O + \dot{C}H_3} \xrightarrow{38} \mathrm{H\dot{C}O + CH_4}$$

The reaction that shows the largest positive sensitivity coefficient, thus inhibiting the overall rate of reaction, is the recombination of methyl radicals, reaction (24). This result is consistent with the major importance of methyl radical branching reactions on the overall radical pool in DME kinetics.

$$\mathrm{CH_3 + CH_3 + (M)} \xrightarrow{-24} \mathrm{C_2H_6 + (M)}$$

In the near-pyrolysis study, the four reactions above account for most of the sensitivity to overall reactivity. (The recombination of a methyl radical with a hydrogen atom also shows a small positive sensitivity coefficient.)

The sensitivity of the overall reaction to hydrogen atoms shows some interesting behaviour. Hydrogen atoms have only a small impact on the overall reactivity, showing little or no sensitivity at low fuel conversion, with modest sensitivity coefficients at higher fuel conversion. Under pyrolysis conditions, there is minimal sensitivity to the chain branching reaction $\dot{H} + O_2 = \dot{O} + \dot{O}H$ thus indicating the O_2 present seems to have very little effect on the overall fuel reactivity. Hydrogen atoms are primarily formed from the decomposition of formyl radicals, produced from formaldehyde. Thus, formaldehyde must be produced in significant concentrations before hydrogen atoms are produced. Under pyrolysis conditions, hydrogen atom abstraction from the fuel, reaction (275), results in a modest increase in overall reactivity, while abstraction from formaldehyde (which competes with abstraction from the fuel) shows a modest positive sensitivity. However, during DME oxidation, hydrogen atom abstraction from the fuel shows a modest positive sensitivity. This is due to the fact that hydrogen atom abstraction from the fuel competes with the chain branching $\dot{H}+O_2 = \dot{O}+\dot{O}H$ reaction, which shows high negative sensitivity coefficients. Hydrogen atom abstraction from formaldehyde shows a positive sensitivity coefficient at 90% fuel conversion and a small negative sensitivity coefficient at 25% fuel conversion. At low fuel conversion, formyl radicals react mainly with molecular oxygen to generate carbon monoxide and a hydroperoxyl radical. The hydroperoxyl radical reacts with a methyl radical to generate a methoxy and a hydroxyl radical. Thus, at low conversion, any potential reduction in overall reactivity by the competing hydrogen atom reaction with formaldehyde is offset by the production of formyl radicals.

There is a large sensitivity to the reactions of methyl radicals with hydroperoxyl radicals, and a modest negative sensitivity to the reaction of methyl radicals with molecular oxygen.

$$\dot{C}H_3 + H\dot{O}_2 \xrightarrow{22} CH_3\dot{O} + \dot{O}H$$

$$\dot{C}H_3 + H\dot{O}_2 \xrightarrow{45} CH_4 + O_2$$

$$\dot{C}H_3 + O_2 \xrightarrow{269} CH_2O + \dot{O}H$$

Reactions (22) and (45) compete with one another. Reaction (22) produces two relatively reactive radicals, while reaction (45) leads to the formation of two stable molecules. The reaction of methyl radical with molecular oxygen also generates a hydroxyl radical, which is more reactive than methyl radical, and thus accelerates the overall reaction rate.

The reaction of the fuel with hydroperoxyl radical also shows a negative sensitivity coefficient. This reaction produces a methoxymethyl radical and hydrogen peroxide. Hydrogen peroxide subsequently decomposes to produce two reactive hydroxyl radicals.

$$CH_3OCH_3 + H\dot{O}_2 \xrightarrow{277} CH_3O\dot{C}H_2 + H_2O_2$$

$$H_2O_2 + (M) \xrightarrow{51} \dot{O}H + \dot{O}H + (M)$$

The self-reaction of hydroperoxyl radicals, reactions (50) and (187) show a positive sensitivity coefficient and thus reduces the overall reactivity of the system. These reactions each

consume two hydroperoxyl radicals and form only one molecule of hydrogen peroxide, ultimately yielding only two reactive hydroxyl radicals. Two hydroperoxyl radicals reacting via reaction (277) above would yield *four* hydroxyl radicals, and thus leads to greater reactivity.

$$H_2O_2 + O_2 \xrightarrow{50} H\dot{O}_2 + H\dot{O}_2$$

$$H_2O_2 + O_2 \xrightarrow{187} H\dot{O}_2 + H\dot{O}_2$$

Finally, under oxidation conditions the β-scission of formyl radicals, reaction (12), shows a positive sensitivity coefficient, while its reaction with molecular oxygen to form carbon monoxide and a hydroperoxyl radical, reaction (46), shows a negative sensitivity coefficient.

$$H\dot{C}O + M \xrightarrow{12} \dot{H} + CO + M$$

$$H\dot{C}O + O_2 \xrightarrow{46} CO + H\dot{O}_2$$

Reaction (46) produces hydroperoxyl radicals that can abstract a hydrogen atom from the fuel, form hydrogen peroxide, and lead to the formation of two hydroxyl radicals or react with methyl radicals to generate methoxy and hydroxyl radicals.

Conclusions

The pyrolysis and oxidation of dimethyl ether has been studied in both an atmospheric-pressure and in a variable-pressure flow reactor. A pyrolysis experiment was performed in the variable-pressure flow reactor at 2.5 atm, at a temperature of 1060 K and with 99.7% nitrogen dilution. A second, near-pyrolysis experiment was carried out in an atmospheric-pressure flow reactor operating at a temperature of 1118 K, with 190 ppm molecular oxygen and 99.6% nitrogen dilution. These pyrolytic experiments were complemented by a set of three oxidation experiments performed in the atmospheric-pressure flow reactor at a temperature of 1086 K, with an approximate nitrogen dilution of 98% and the equivalence ratio varying in the range $0.32 \leq \phi \leq 3.4$. In all experiments, species concentrations, measured using FTIR, were correlated against residence time.

All experiments were simulated using a detailed chemical kinetic mechanism. The detailed kinetic model is able to reproduce the fuel, oxygen and intermediate product species profiles with a high degree of accuracy, with the exception of the lean oxidation experiment where the concentration of methane is under-predicted by about a factor of three, Fig. 12. Modeling results indicate that, under all conditions, the most important initiation reaction for dimethyl ether, is its unimolecular decomposition to form methoxy and methyl radicals. The methyl radical so produced, can abstract a hydrogen atom from the fuel to generate methoxymethyl radical and methane, with methoxy radical either decomposing to form formaldehyde and hydrogen atom or reacting with molecular oxygen to yield formaldehyde and hydroxyl radical. Methoxymethyl radicals decompose to generate formaldehyde and a methyl radical. Thus, the methyl radical plays a very important role in dimethyl ether pyrolysis and oxidation. In addition, the formaldehyde submechanism is a very important subset of the overall DME mechanism.

Acknowledgements

The experimental work discussed in this paper and computational work appearing in the thesis of S. Fischer, were conducted at Princeton University. The U.S. Department of Energy, Chemical Sciences Division, Office of Basic Energy Sciences, supported these contributions, and those of Prof. Dryer, under Contract No. DE-FG02-86ER-13503. S. Fischer also wishes to acknowledge the support of her thesis research under the National Defense Fellowship Program. Mr. Paul Michniewicz, Mrs. Yolanda Stein, Mr. Joe Sivo and Dr. Steve Klotz are acknowledged for their assistance in completing the experimental portions of the work. The authors also acknowledge helpful comments and discussions with Dr. W. J. Pitz and Dr. C. K. Westbrook. The computations appearing in this paper and the contributions of Dr. Curran were performed under the auspices of the U.S. Department of Energy by the Lawrence Livermore National Laboratory under contract No. W–7405–ENG–48.

References

[1] C. J. Green, N. A. Cockshutt and L. King, Society of Automotive Engineers publication SAE–902155 (1990).

[2] M. Karpuk, J. D. Wright, J. L. Dippo and D. E. Jansen, Society of Automotive Engineers publication SAE–912420 (1991).

[3] T. H. Fleisch, C. Mc Carthy, A. Basu and C. Udovich, Society of Automotive Engineers publication SAE–950061 (1995).

[4] A. M. Rouhi, *Chem. and Eng. News.* pp. 37–39, May 29, (1995).

[5] R. Brooks, WARD's *Engine and Vehicle Tech. Update* p. 3, July 15, (1995).

[6] T. H. Fleisch, In *AVL Conference* "Engine and Environment 1995" Graz, Austria, 1995.

[7] S. M. Japar, T. J. Wallington, J. F. O. Richert and J. C. Ball, *Int. J. Chem. Kinet.* 22:1257–1269 (1990).

[8] S. M. Japar, T. J. Wallington, S. J. Rudy and T. Y. Chang, *Envir. Sci. Tech.* 25:410–415 (1991).

[9] P. Dagaut, P, J.-C. Boettner and M. Cathonnet, *Twenty-Sixth Symposium (International) on Combustion.*, The Combustion Institute, Pittsburgh, 1996, pp. 627–632.

[10] U. Pfahl, K. Fieweger and G. Adomeit, *Twenty-Sixth Symposium (International) on Combustion.*, The Combustion Institute, Pittsburgh, 1996, pp. 781–789.

[11] H. J. Curran, W. J. Pitz, C. K. Westbrook, P. Dagaut, J-C. Boettner and M. Cathonnet, *Int. J. Chem. Kinet.* 30:229–241 (1998).

[12] P. Dagaut, C. Daly, J. M. Simmie and M. Cathonnet, *Twenty-Seventh Symposium (International) on Combustion.*, The Combustion Institute, Pittsburgh, 1998, pp. 361–369.

[13] M. U. Alzueta, J. Muro, R. Bilbao and P. Glarborg, *Israel J. Chem.* 39:73–86 (1999).

[14] T. Amano and F. L. Dryer, *Twenty–Seventh Symposium (International) on Combustion*, Combustion Institute, Pittsburgh, 1998, pp. 397–404.

[15] H. J. Curran, S. L. Fischer and F. L. Dryer, *Int. J. Chem. Kinet.* submitted, (1999).

[16] L Crocco, I. Glassman and I. E. Smith, *Jet. Propulsion* 12:66 (1957).

[17] R. A. Yetter, F. L. Dryer and H. Rabitz, *Combust. Sci. and Tech.* 79:129–140 (1991).

[18] J. F. Roesler, R. A. Yetter and F. L. Dryer, *Combust. Flame.* 100:495–504 (1995).

[19] J. V. Seeley, J. T. Jayne and M. J. Molina, *Int. J. Chem. Kinet.* 25:571 (1993).

[20] S. Hochgreb and F. L. Dryer, *J. Phys. Chem.* 96:295 (1992).

[21] R. A. Yetter and F. L. Dryer, *Twenty-Fourth Symposium (International) on Combustion.*, The Combustion Institute, Pittsburgh, 1992, p. 757.

[22] M. T. Allen, R. A. Yetter and F. L. Dryer, *Int. J. Chem. Kinet.* 27:883 (1995).

[23] M. A. Mueller, R. A. Yetter and F. L. Dryer, *Twenty-Seventh Symposium (International) on Combustion.*, The Combustion Institute, Pittsburgh, 1998, pp. 177–184.

[24] T. J. Held, Ph. D. Thesis, Department of Mechanical and Aerospace Engineering, Princeton University, Princeton, NJ, October, 1993. MAE 1978-T.

[25] C. V. Callahan, T. J. Held, F. L. Dryer, R. Minetti, M. Ribancour, L. R. Sochet, T. Faravelli, P. Gaffuri and E. Ranzi, *Twenty-Sixth Symposium (International) on Combustion.*, The Combustion Institute, Pittsburgh, 1996, pp. 739–746.

[26] H. J. Curran, W. J. Pitz, C. K. Westbrook, C. V. Callahan and F. L. Dryer, *Twenty-Seventh Symposium (International) on Combustion.*, The Combustion Institute, Pittsburgh, 1998, pp. 379–387.

[27] M. L. Vermeersch, Ph. D. Thesis, Department of Mechanical and Aerospace Engineering, Princeton University, Princeton, NJ, August, 1991. MAE 1916-T.

[28] F. L. Dryer, Ph. D. Thesis, Department of Aerospace and Mechanical Sciences, Princeton University, Princeton, NJ, March, 1972. AMS-T-1034.

[29] J. L. Emdee, K. Brezinsky and I. Glassman, *J. Phys. Chem.* 95:1626–1635 (1991).

[30] C. M. Lund and L. Chase, "HCT - A General Computer Program for Calculating Time-Dependent Phenomena Involving One-Dimensional Hydrodynamics, Transport, and Detailed Chemical Kinetics," Lawrence Livermore National Laboratory report UCRL-52504, revised (1995).

[31] T. J. Kim, R. A. Yetter and F. L. Dryer, *Twenty-Fifth Symposium (International) on Combustion*, The Combustion Institute, Pittsburgh, 1994, p. 759.

[32] C. K. Westbrook and F. L. Dryer, *Prog. Energ. Sci. Combust.* 10:1 (1984).

[33] E. R. Ritter and J. W. Bozzelli, *Int. J. Chem. Kinet.* 23:767 (1991).

[34] T. Lay, J. W. Bozzelli, A. M. Dean and E. R. Ritter, *J. Phys. Chem.* 99:14514 (1995).

[35] M. A. Mueller, T. J. Kim, R. A. Yetter and F. L. Dryer, *Int. J. Chem. Kinet.* 31:113–125 (1999).

[36] S. Hochgreb, R. A. Yetter and F. L. Dryer, *Twenty-Third Symposium (International) on Combustion*, Combustion Institute, Pittsburgh, 1990, pp. 171–177.

[37] S. Hochgreb and F. L. Dryer, *Combust. Flame* 91:257–284 (1992).

[38] N. M. Marinov, W. J. Pitz, C. K. Westbrook, M. J. Castaldi and S. M. Senkan, *Combust. Sci. and Tech.* 116–117:211–287 (1996).

[39] J. Warnatz, In Gardiner Jr., W. C. (Ed.), *Combustion Chemistry*. Springer-Verlag, New York, 1984, pp. 197–360.

[40] W. Tsang and R. F. Hampson, *J. Phys. Chem. Ref. Data* 15:1087–1279 (1986).

[41] J. V. Michael, D. G. Keil and R. B. Klemm, *Int. J. Chem. Kinet.* 15:705–719 (1983).

[42] D. L. Baulch, C. J. Cobos, R. A. Cox, C. Esser, P. Frank, Th., Just, J. A. Kerr, M. J. Pilling, J. Troe, R. W. Walker and J. Warnatz, *J. Phys. Chem. Ref. Data* 21:411–429 (1992).

[43] A. N. Pirraglia, J. V. Michael, J. W. Sutherland and R. B. Klemm, *J. Phys. Chem.* 93:282–291 (1989).

[44] J. W. Sutherland, J. V. Michael, A. N. Pirraglia, F. L. Nesbitt and R. B. Klemm, *Twenty-First Symposium (International) on Combustion*, Combustion Institute, Pittsburgh, PA, 1986, pp. 929–941.

[45] J. W. Sutherland, P. M. Patterson and R. B. Klemm, *Twenty-First Symposium (International) on Combustion*, Combustion Institute, Pittsburgh, PA, 1990, pp. 51–57.

[46] J. V. Michael and J. W. Sutherland, *J. Phys. Chem.* 92:3853–3857 (1988).

[47] R. S. Timonen, E. Ratajczak, D. Gutman and A. F. Wagner, *J. Phys. Chem.* 91:5325 (1987).

[48] H. Hippler, H. Neunaber and J. Troe, *J. Chem. Phys. Lett.* 192(4):333–337 (1992).

[49] T. J. Held and F. L. Dryer, *Int. J. Chem. Kinet.* 30:805–830 (1998).

[50] M. Cathonnet, J-C. Boettner and H. James, *J. Chim. Phys.* 79:475 (1982).
[51] J. W. Bozzelli and A. M. Dean, *J. Phys. Chem.* 94:3313 (1990).
[52] F. P. Tully, A. T. Droege, M. L. Koszykowski and C. F. Melius, *J. Phys. Chem.* 90:691 (1986).
[53] J. T. Herron, *J. Phys. Chem. Ref. Data* 17:967 (1988).
[54] D. Walter, H-H. Grotheer, J. W. Davies, M. J. Pilling and A. F. Wagner, *Twenty–Third Symposium (International) on Combustion*, Combustion Institute, Pittsburgh, 1990, p. 107.
[55] R. S. Timonen, E. Ratajczak and D. Gutman, *J. Phys. Chem.* 91:692 (1987).
[56] B. Eiteneer, C.-L. Yu, M. Goldenberg and M. Frenklach, *J. Phys. Chem.* A, 102:5196–5205 (1998).
[57] R. Humpfer, H. Oser, H-H. Grotheer and Th. Just, *Twenty–Fifth Symposium (International) on Combustion*, Combustion Institute, Pittsburgh, 1994, p. 721.
[58] N. M. Marinov and P. C. Malte, *Int. J. Chem. Kinet.* 27:957 (1995).
[59] M. Page, M. C. Lin, Y. He and T. K. Choudhury, *J. Phys. Chem.* 93:4404 (1989).
[60] Th. Just, P. Roth and R. Damm, *Sixteenth Symposium (International) on Combustion*, Combustion Institute, Pittsburgh, 1977, p. 961.
[61] D. L. Baulch, C. J. Cobos, R. A. Cox, P. Frank, G. Hayman, Th. Just, J. A. Kerr, T. Murrells, M. J. Pilling, J. Troe, R. W. Walker and J. Warnatz, *J. Phys. Chem. Ref. Data* 23:847–1033 (1994).
[62] R. S. Timonen, *Ann. Acad. Sci. Fenn.* Ser. A2 218:5 (1988).
[63] H. Hippler, J. Troe and J. Willner, *J. Chem. Phys.* 93:1755–1760 (1990).
[64] N. M. Marinov, C. K. Westbrook and W. J. Pitz, Transport Phenomena in Combustion, 1995, pp. 118–129.
[65] S. H. Robertson, P. W. Seakins and M. J. Pilling, In Pilling, M. J. (Ed.), *Chemical Kinetics*. Elsevier, New York, 1997, pp. 125–234.
[66] C. K. Westbrook, Estimated in CDAT data base.
[67] C. K. Westbrook, M. M. Thornton, W. J. Pitz and P. C. Malye, *Twenty–Second Symposium (International) on Combustion*, Combustion Institute, Pittsburgh, 1988, p. 863.
[68] J. A. Miller and C. F. Melius, *Combust. Flame* 91:21 (1992).
[69] J. F. Bott and N. Cohen, *Int. J. Chem. Kinet.* 23:1075 (1991).
[70] T. J. Held and F. L. Dryer, *Twenty-Fifth Symposium (International) on Combustion*, Combustion Institute, Pittsburgh, 1994, p. 901.
[71] W. Tsang, *J. Phys. Chem. Ref. Data* 16:471–508 (1987).
[72] E. W. Kaiser, *J. Phys. Chem.* 94:4493–4499 (1990).
[73] J. V. Michael, D. F. Nava, W. A. Payne and L. J. Stief, *J. Chem. Phys.* 70:5222–5227 (1979).
[74] J. Peeters, W. Boullart and K. Devriendt, *J. Phys. Chem.* 99:3583 (1995).
[75] M. J. Kurylo, N. C. Peterson and W. Braun, *J. Chem. Phys.* 53:2776 (1970).
[76] N. M. Marinov, *Int. J. Chem. Kinet.* 31:183–220 (1999).
[77] A. Liu, C. D. Jonah and W. A. Mulac, *Radiat. Phys. Chem.* 34:687–691 (1989).

[78] P. H. Taylor, M. S. Rahman, M. Arif, B. Dellinger and P. Marshall, *Twenty-Sixth Symposium (International) on Combustion*, Combustion Institute, Pittsburgh, 1996, pp. 497–504.

[79] D. A. Whytock, J. V. Michael, W. A. Payne and L. J. Stief, *J. Chem. Phys.* 65:4871 (1976).

[80] D. Hartmann, J. Karthauser, J. P. Sawerysyn and R. Zellner, *Ber. Bunsenges. Phys. Chem.* 94:639 (1990).

[81] I. Oref and B. S. Rabinovitch, *J. Phys. Chem.* 72:4488 (1970).

[82] P. D. Lightfoot, P. Roussel, F. Caralp and R. Lesclaux, *J. Chem. Soc. Faraday Trans.* 87:3213–3220 (1991).

[83] K. A. Sahetchian, R. Rigny, R., J. Tardieu De Maleissye, L. Batt, M. Anwar Khan, and S. Mathews, *Twenty-Fourth Symposium (International) on Combustion*, Combustion Institute, Pittsburgh, 1992, pp. 637–643.

[84] A. Lifshitz and H. Ben-Hamou, *J. Phys. Chem.* 87:1782 (1983).

[85] R. R. Baldwin, A. Keen and R. W. Walker, *J. Chem. Soc. Faraday Trans.* 1, 80:435 (1984).

[86] A. C. Brown, C. E. Canosa-Mas, A. D. Parr and R. P. Wayne, *Chem. Phys. Lett.* 161:491 (1989).

[87] J. P. Hessler, H. Du, P. J. Ogren and A. F. Wagner, 14th Intl. Symposium on Gas Kinetics, Sept. 7-13, 1996, Leeds, UK.

[88] Y. Hidaka, T. Nakamura, H. Tanaka, K. Inami and H. Kawano, *Int. J. Chem. Kinet.* 22:701 (1990).

[89] L. F. Loucks and K. J. Laidler, *Can. J. Chem.* 45:2767–2773 (1967).

[90] B. Veyret, P. Roussel and R. Lesclaux, *Int. J. Chem. Kinet.* 16:1559–1608 (1984).

[91] D. S. Y. Hsu, W. M. Shaub, M. Blackburn and M. C. Lin, *Nineteenth Symposium (International) on Combustion*, Combustion Institute, Pittsburgh, 1982, p. 89.

[92] P. Dagaut, T. J. Wallington and M. J. Kurylo, *J. Photochem. Photobiol. A. Chem.* 48:187 (1989).

[93] M. E. Jenkin, G. D. Hayman, T. J. Wallington, R. D. Hurley, J. C. Ball, O. J. Nielsen and T. Ellermann, *J. Phys. Chem.* 97:11712–11723, (1993).

[94] R. R. Baldwin, C. E. Dean, and R. W. Walker, *J. Chem. Soc. Faraday Trans.* 2, 82:1445 (1986).

[95] W. G. Mallard, F. Westley, J. T. Herron and R. F. Hampson, NIST Chemical Kinetics Database - Ver. 6.0, NIST Standard Reference Data, Gaithersburg, MD (1994).

[96] E. A. Irdam, J. H. Kiefer, L. B. Harding and A. F. Wagner, *Int. J. Chem. Kinet.* 25:285–303 (1993).

[97] R. W. Walker, In Ashmore, G. (Ed.), *Reaction Kinetics*. Chemical Society, Burlington House, London, 1975, pp. 161–211.

[98] R. W. Walker, *Twenty Second Symposium (International) on Combustion*, Combustion Institute, Pittsburgh, 1988, pp. 883–892.

[99] A. M. Dean, *J. Phys. Chem.* 89:4600 (1985).

[100] A. M. Dean, J. M. Bozzelli and E. R. Ritter, *Combust. Sci. Tech.* 80:63–85 (1991).

[101] P. D. Pacey, *Can. J. Chem.* 53:2742–2747 (1975).

[102] D. Aronowitz and D. Naegeli, *Int. J. Chem. Kinet.* 9:471–479 (1977).
[103] L. Batt, G. Alvarado-Salinas, I. A. B. Reid, C. Robinson and D. B. Smith, *Twenty Fifth Symposium (International) on Combustion*, Combustion Institute, Pittsburgh, 1982, p. 81.
[104] J. F. Meagher, P. Kim, J. H. Lee and R. B. Timmons, *J. Phys. Chem.* 78:2650–2657 (1974).
[105] C. Faubel, K. Hoyermann, E. Strofer and H. Gg. Wagner, *Ber. Bunsenges. Phys. Chem.* 83:532 (1979).
[106] J. H. Lee, R. C. Machen, D. F. Nava and L. J. Stief, *J. Chem. Phys.* 74:2839 (1981).
[107] N. L. Arthur, P. Gray and A. A. Herod, *Can. J. Chem.* 47:1347 (1969).
[108] P. Gray and A. A. Herod, *Trans. Faraday Soc.* 64:2723 (1968).
[109] K. C. Manthorne and P. D. Pacey, *Can. J. Chem.* 56:1307–1310 (1978).
[110] T. K. Choudhury, W. A. Sanders and M. C. Lin, *J. Phys. Chem.* 93:5143 (1989).
[111] T. K. Choudhury and W. A. Sanders, *J. Chem. Soc. Faraday Trans.* 2 85:801 (1989).
[112] C. Anastasi, *J. Chem. Soc. Faraday Trans.* 1 79:749 (1983).
[113] W. Tsang, *J. Phys. Chem. Ref. Data* 16:471 (1987).
[114] H. F. LeFevre, J. F. Meagher and R. B. Timmons, *Int. J. Chem. Kinet.* 4:103 (1972).
[115] C. Faubel, K. Hoyermann and H. Gg. Wagner, *Z. Phys. Chem. (Neue Folge)* 130:1 (1982).
[116] Y. Mirokhin, W. G. Mallard, F. Westley, J. T. Herron, D. Frizzell and R. Hampson, NIST Standard Reference Database 17-2Q98, Gaithersburg, MD (1998).
[117] M. Arif, B. Dellinger and P. H. Taylor, *J. Phys. Chem.* 101:2436–2441 (1997).
[118] A. Mellouki, S. Teton and G. LeBras, *Int. J. Chem. Kinet.* 27:791–805 (1995).
[119] L. Nelson, O. Rattigan, R. Neavyn and H. Sidebottom, *Int. J. Chem. Kinet.* 22:1111 (1990).
[120] T. J. Wallington, J. M. Andino, L. M. Skewes, W. O. Siegl and S. M. Japar, *Int. J. Chem. Kinet.* 21:993 (1989).
[121] F. P. Tully and A. T. Droege, *J. Phys. Chem.* 19:251–259 (1987).
[122] S. W. Benson, *Thermochemical Kinetics*. John Wiley and Sons, Inc., New York 1976.
[123] J. W. Bozzelli, and W. J. Pitz, *Twenty Fifth Symposium (International) on Combustion*, Combustion Institute, Pittsburgh, 1994, p. 783.
[124] H. J. Curran, P. Gaffuri, W. J. Pitz and C. K. Westbrook, *Combust. Flame* 114:149–177 (1998).
[125] D. Walter, H-H. Grotheer, J. W. Davies, M. J. Pilling and A. F. Wagner, *Twenty-Third Symposium (International) on Combustion*, Combustion Institute, Pittsburgh, 1991, p. 107.
[126] H. J. Curran, J. M. Simmie, P. Dagaut, D. Voisin and M. Cathonnet, *Twenty-Sixth Symposium (International) on Combustion*, Combustion Institute, Pittsburgh, 1996, pp. 613–620.
[127] F. Slemr and P. Warneck, *Int. J. Chem. Kinet.* 9:267 (1977).
[128] L. F. Loucks, *Can. J. Chem.* 45:2775 (1967).
[129] S. Dobe, C. Oehlers, F. Temps, H. Gg. Wagner and H. Zimer, *Ber. Bunsenges. Phys. Chem.* 98:754–757 (1994).

[130] Y. Hidaka, T. Taniguchi, H. Tanaka, T. Kamesawa, K. Inami and H. Kawano, *Combust. Flame* 92:365–376 (1993).

[131] T. K. Choudhury and M. C. Lin, *Combust. Sci. Technol.* 64:19–28 (1989).

[132] R. B. Klemm, *J. Chem. Phys.* 71:1987 (1979).

[133] Th. Just, *Seventeenth Symposium (International) on Combustion*, Combustion Institute, Pittsburgh, 1979, pp. 584–585.

[134] V. A. Nadtochenko, O. M. Sarkisov and V. I. Vedeneev, *Dokl. Phys. Chem.* (Eng. Transl.) 243:418 (1978).

[135] A. A. Westenberg and N. DeHaas, *J. Phys. Chem.* 76:2213 (1972).

[136] B. A. Ridley, J. A. Davenport, L. J. Stief and K. H. Welge, *J. Chem. Phys.* 57:520 (1972).

[137] R. Klein, M. D. Scheer and L. J. Schoen, *J. Am. Chem. Soc.* 78:50 (1956).

Species	H_f° @ 298 K (kcal/mol)	S_f° @ 298 K (cal/mol-K)	C_p @ 300 K (cal/mol-K)
CH_3OCH_3	-43.4	63.8	15.8
$CH_3O\dot{C}H_2$	1.0	67.3	16.3
$CH_3OCH_2O_2H$	-68.4	83.8	24.0
$CH_3OCH_2\dot{O}$	-34.5	73.9	18.4
CH_3OCHO	-84.4	71.5	17.1
$CH_3OCH_2\dot{O}_2$	-34.6	82.6	21.9
$\dot{C}H_2OCH_2O_2H$	-24.0	85.9	24.5
$\dot{O}_2CH_2OCH_2O_2H$	-59.6	101.2	30.1
$HO_2CH_2O\dot{C}HO_2H$	-51.9	108.3	32.4
HO_2CH_2OCHO	-109.4	90.1	25.3
$\dot{O}CH_2OCHO$	-75.5	80.3	19.6
$HOCH_2O\dot{C}O$	-81.5	101.3	22.9
$HOCH_2\dot{O}$	-43.4	64.8	13.1
HOCHO	-90.2	59.4	10.8

Table 2: Thermodynamic properties for selected species

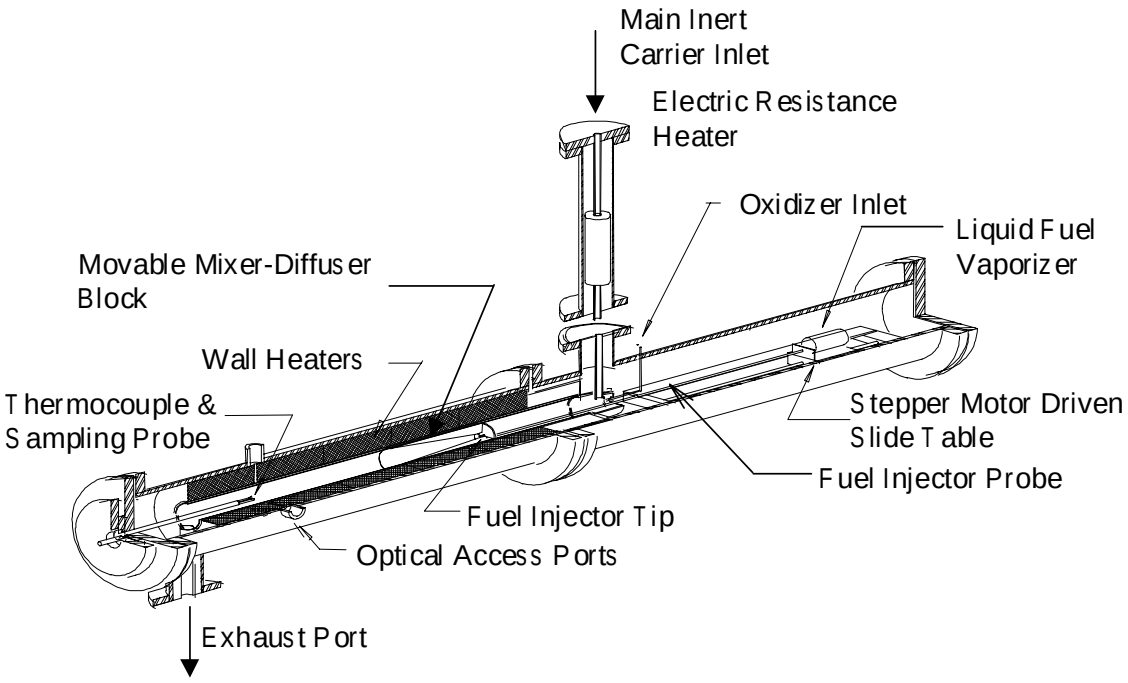

Figure 1: Princeton Variable-Pressure Flow Reactor and Mixer Block Assembly.

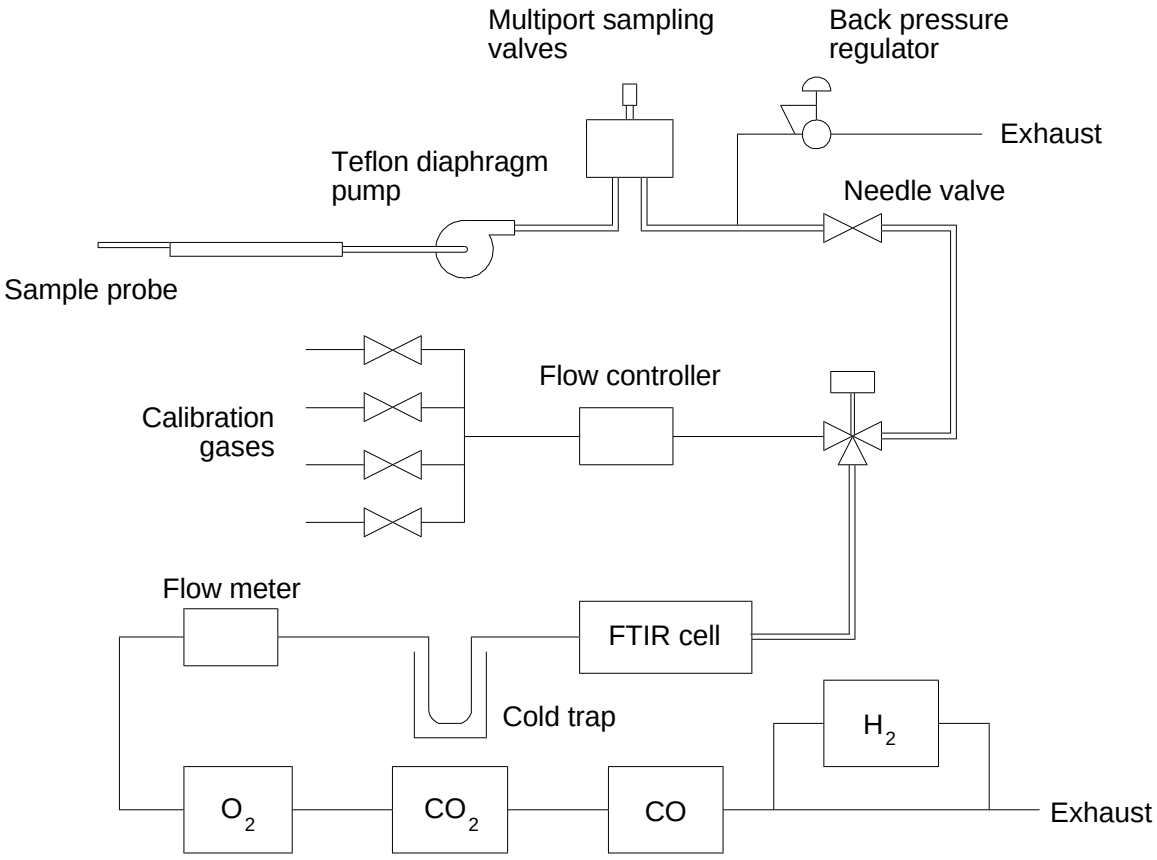

Gas Sampling System (All transfer lines to FTIR heated)

Figure 2: Gas Sampling System.

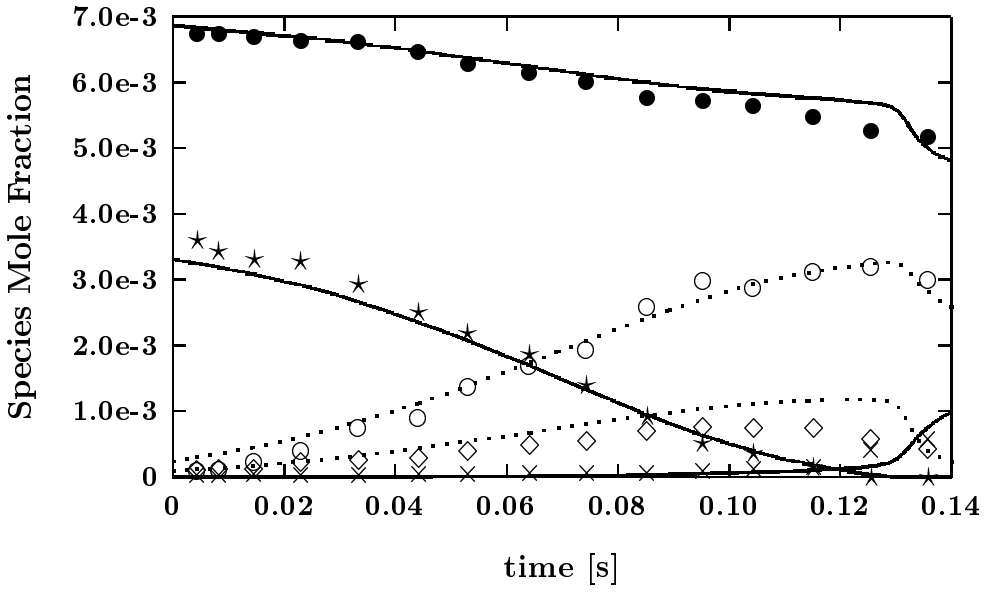

Figure 3: Measured [36, 37] (symbols) and calculated (curves) species concentrations from a flow reactor oxidation. 3560 ppm CH_2O, $\phi = 0.5$, P=1.0 atm, T=944 K. • O_2, ∘ CO, ⋆ CH_2O, ◇ H_2 and × CO_2. $\tau_{\text{offset}} = -0.075$ s. Dotted lines correspond to open symbols.

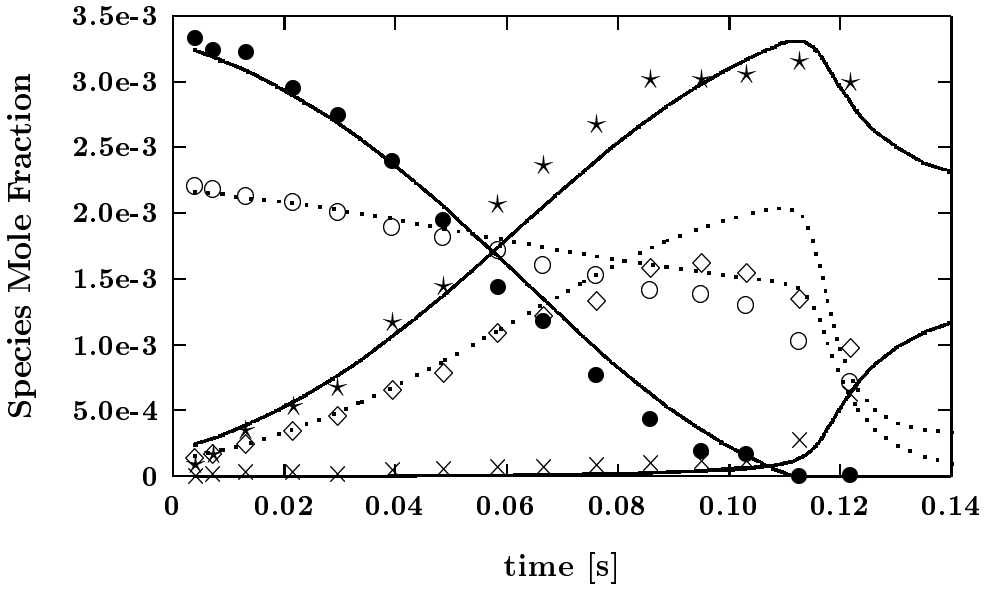

Figure 4: Measured (symbols) [36, 37] and calculated (curves) species concentrations from a flow reactor oxidation. 3480 ppm CH_2O, $\phi = 1.56$, P=1.0 atm, T=945 K. • CH_2O, ∘ O_2, ⋆ CO, ◇ H_2 and × CO_2. $\tau_{\text{offset}} = -0.07$ s. Dotted lines correspond to open symbols.

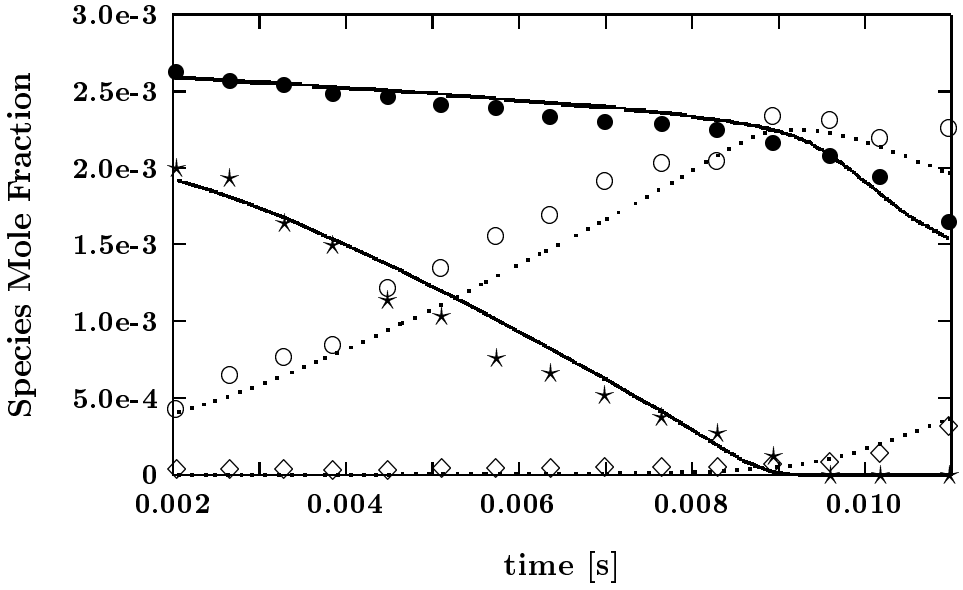

Figure 5: Measured (symbols) [36, 37] and calculated (curves) species concentrations from a flow reactor oxidation. 2340 ppm CH_2O, $\phi = 0.88$, P=1.0 atm, T=1095 K. • O_2, ∘ CO, ⋆ CH_2O, and ◇ CO_2. $\tau_{\text{offset}} = -0.01$ s. Dotted lines correspond to open symbols.

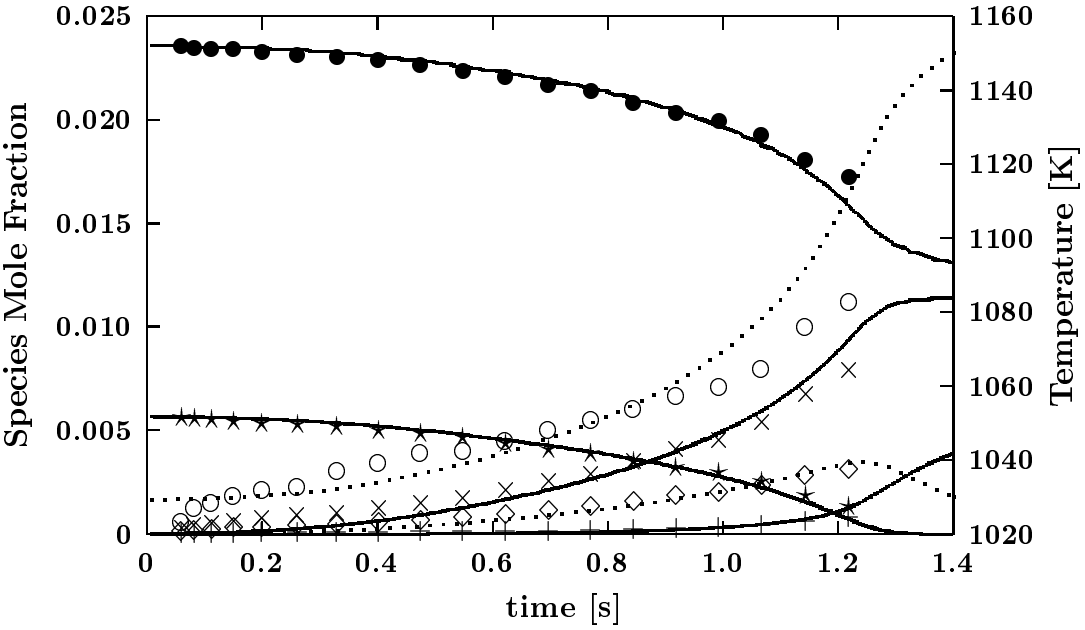

Figure 6: Measured (symbols) [14] and calculated (curves) species concentrations from a flow reactor oxidation. 5700 ppm CH_4, $\phi = 0.5$, P=10 atm, T=1029 K. • O_2, ∘ Temperature, ⋆ CH_4, × H_2O, ◇ CO, and + CO_2. $\tau_{\text{offset}} = -0.1$ s. Dotted lines correspond to open symbols.

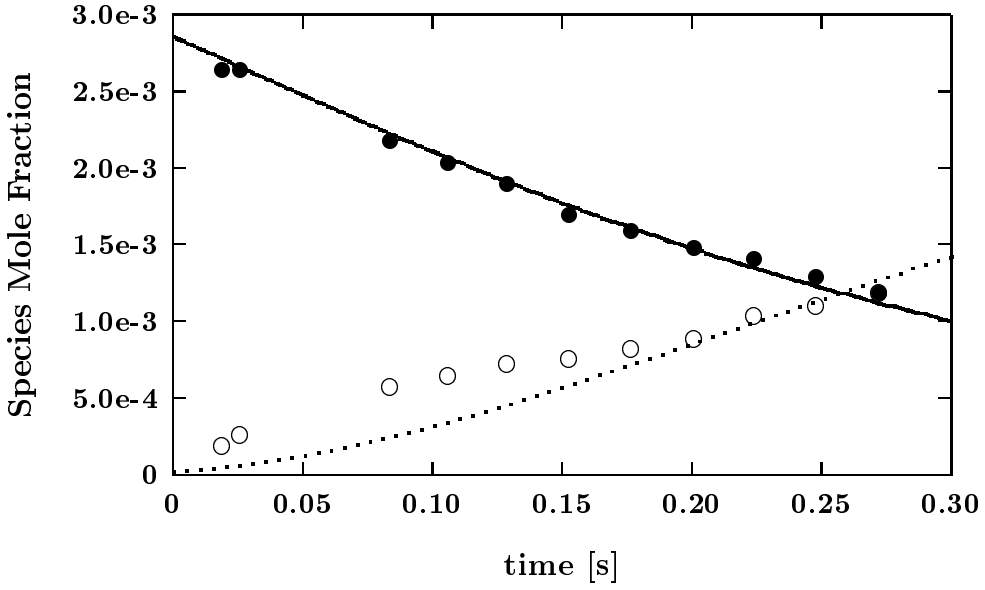

Figure 7: Measured (symbols) and calculated (curves) species concentrations from a flow reactor pyrolysis. 3090 ppm DME, P=2.5 atm, T=1060 K. • CH_3OCH_3, and ∘ CO. $\tau_{\text{offset}} = -0.05$ s. Dotted lines correspond to open symbols.

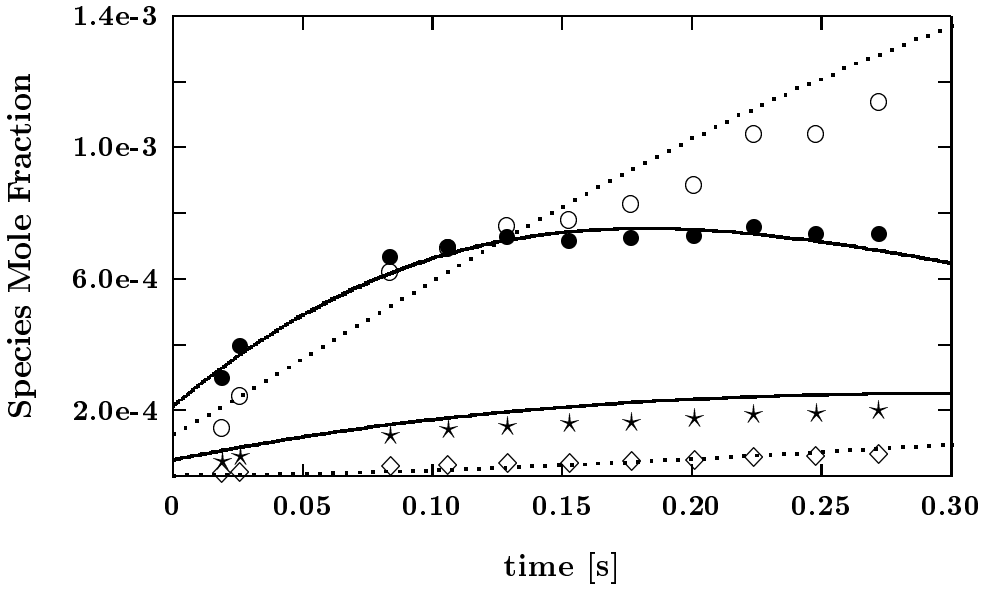

Figure 8: Measured (symbols) and calculated (curves) species concentrations from a flow reactor pyrolysis. 3090 ppm DME, P=2.5 atm, T=1060 K. • CH_2O, ∘ CH_4, ⋆ C_2H_6, and ◇ C_2H_4. $\tau_{\text{offset}} = -0.05$ s. Dotted lines correspond to open symbols.

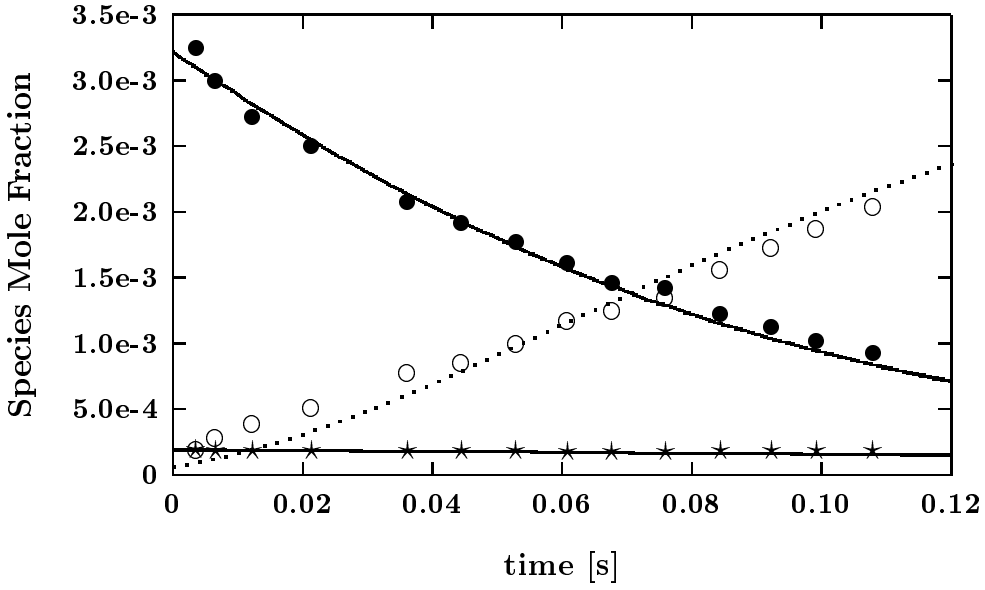

Figure 9: Measured (symbols) and calculated (curves) species concentrations from a flow reactor near-pyrolysis. 3740 ppm DME, P=1.0 atm, T=1118 K. • CH_3OCH_3, ○ CO, and ⋆ O_2. $\tau_{\text{offset}} = -0.015$ s. Dotted lines correspond to open symbols.

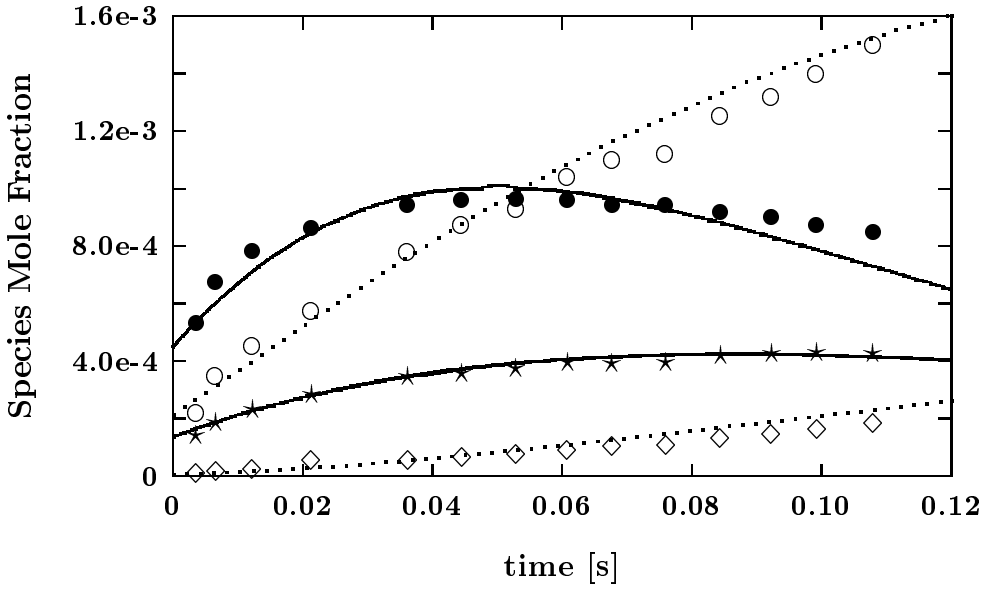

Figure 10: Measured (symbols) and calculated (curves) species concentrations from a flow reactor near-pyrolysis. 3740 ppm DME, P=1.0 atm, T=1118 K. • CH_2O, ○ CH_4, ⋆ C_2H_6, and ◇ C_2H_4. $\tau_{\text{offset}} = -0.015$ s. Dotted lines correspond to open symbols.

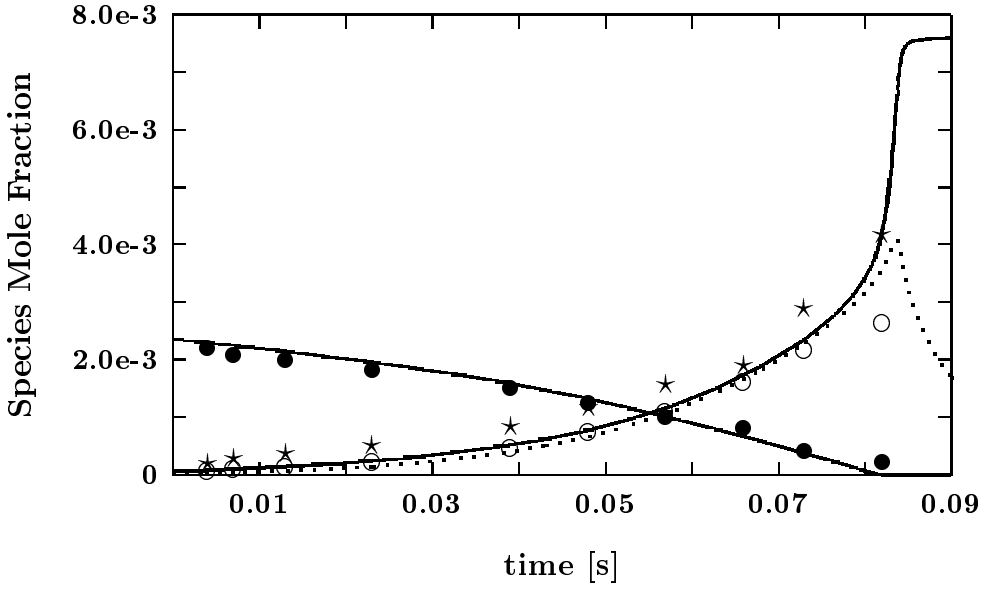

Figure 11: Measured (symbols) and calculated (curves) species concentrations from a flow reactor oxidation. 2560 ppm DME, $\phi = 0.3$, P=1.0 atm, T=1086 K. • CH_3OCH_3, ○ CO and ⋆ H_2O. $\tau_{\text{offset}} = -0.018$ s. Dotted lines correspond to open symbols.

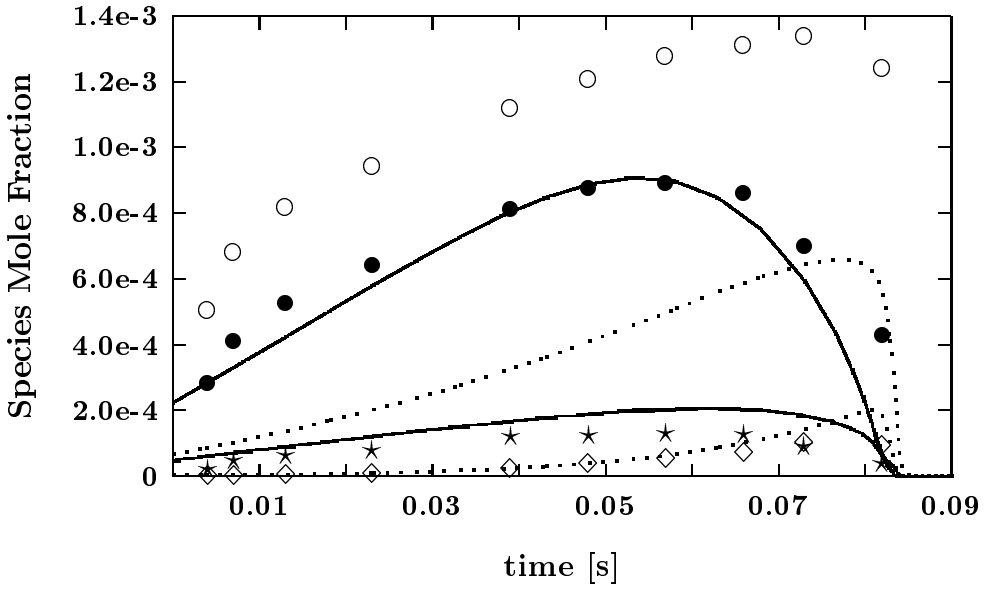

Figure 12: Measured (symbols) and calculated (curves) species concentrations from a flow reactor oxidation. 2560 ppm DME, $\phi = 0.3$, P=1.0 atm, T=1086 K. • CH_2O, ○ CH_4, ⋆ C_2H_6, and ◇ C_2H_4. $\tau_{\text{offset}} = -0.018$ s. Dotted lines correspond to open symbols.

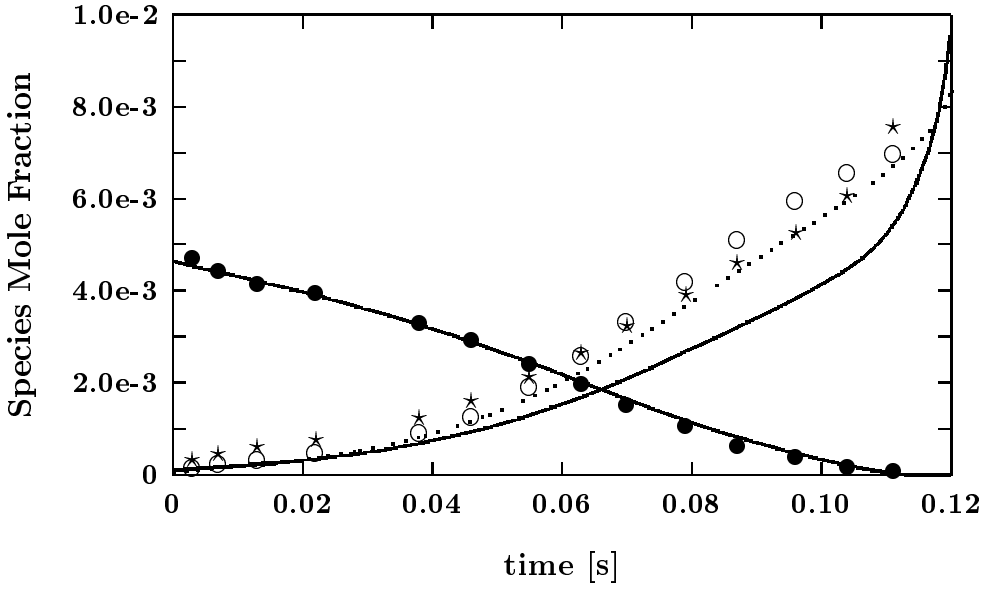

Figure 13: Measured (symbols) and calculated (curves) species concentrations from a flow reactor oxidation. 5270 ppm DME, $\phi = 1.06$, P=1.0 atm, T=1084 K. • CH_3OCH_3, ∘ CO and ⋆ H_2O. $\tau_{\text{offset}} = -0.03$ s. Dotted lines correspond to open symbols.

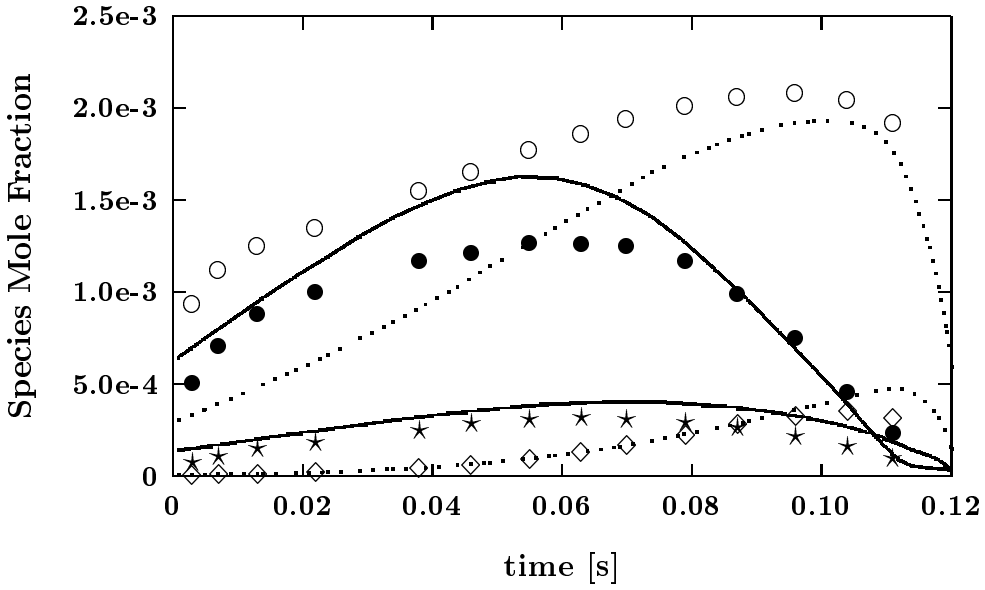

Figure 14: Measured (symbols) and calculated (curves) species concentrations from a flow reactor oxidation. 5270 ppm DME, $\phi = 1.06$, P=1.0 atm, T=1084 K. • CH_2O, ∘ CH_4, ⋆ C_2H_6, and ◇ C_2H_4. $\tau_{\text{offset}} = -0.03$ s. Dotted lines correspond to open symbols.

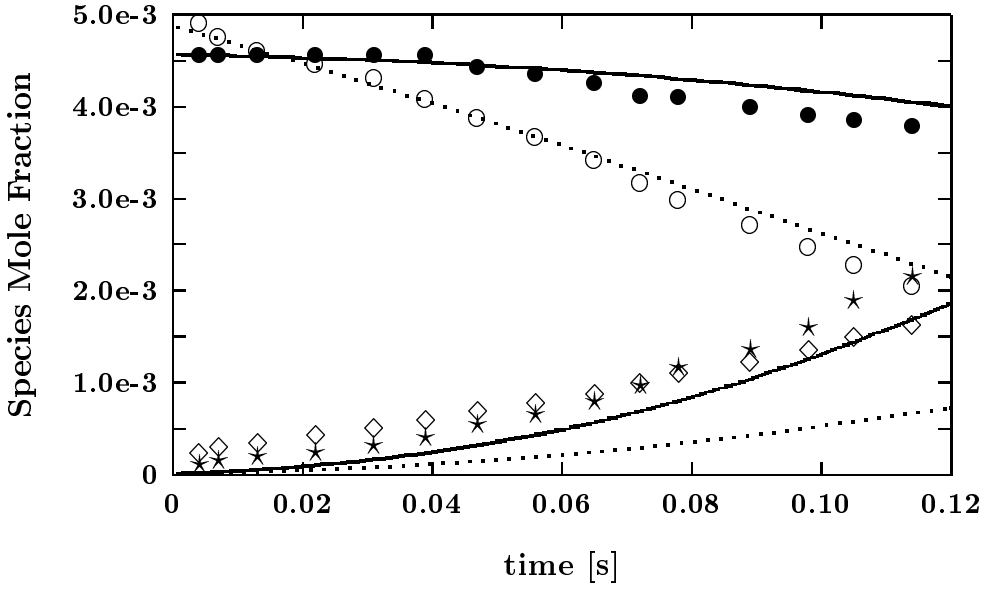

Figure 15: Measured (symbols) and calculated (curves) species concentrations from a flow reactor oxidation. 5160 ppm DME, $\phi = 3.4$, P=1.0 atm, T=1080 K. • O_2, ○ CH_3OCH_3, ⋆ CO and ◇ H_2O. $\tau_{\text{offset}} = -0.018$ s. Dotted lines correspond to open symbols.

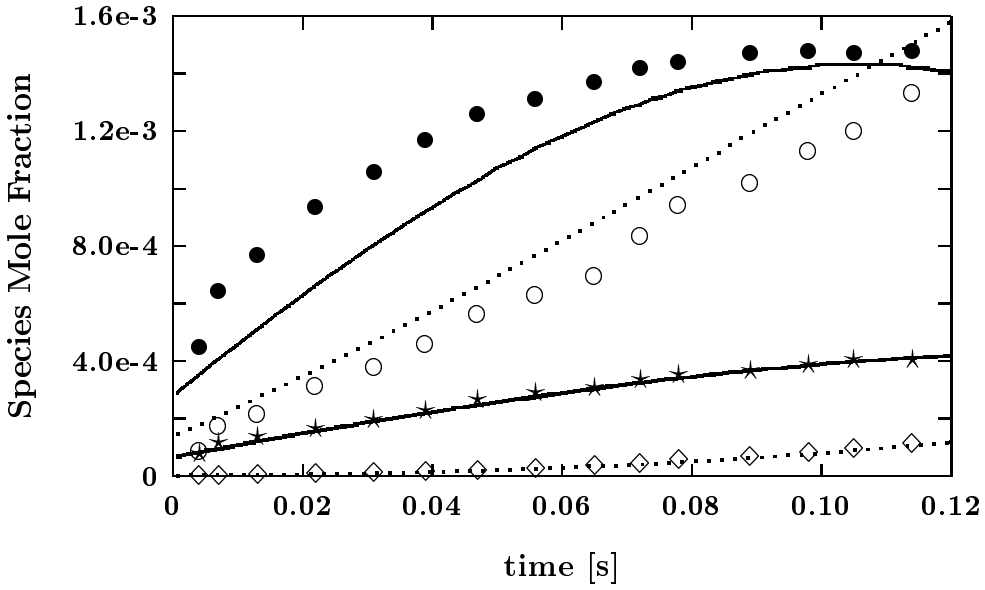

Figure 16: Measured (symbols) and calculated (curves) species concentrations from a flow reactor oxidation. 5160 ppm DME, $\phi = 3.4$, P=1.0 atm, T=1080 K. • CH_2O, ○ CH_4, ⋆ C_2H_6, and ◇ C_2H_4. $\tau_{\text{offset}} = -0.018$ s. Dotted lines correspond to open symbols.

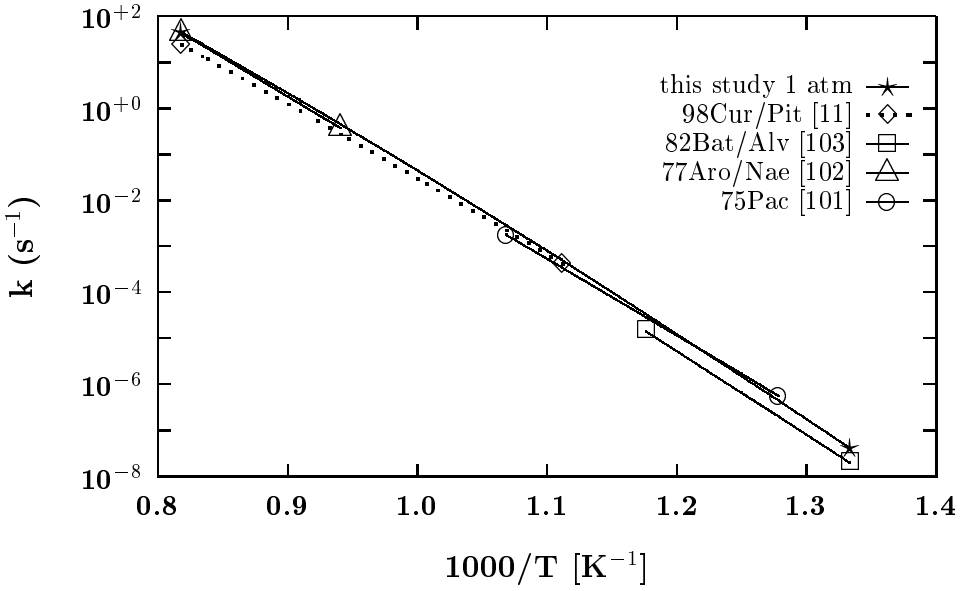

Figure 17: Arrhenius plot of rate constant expressions for $CH_3OCH_3 = CH_3\dot{O} + \dot{C}H_3$.

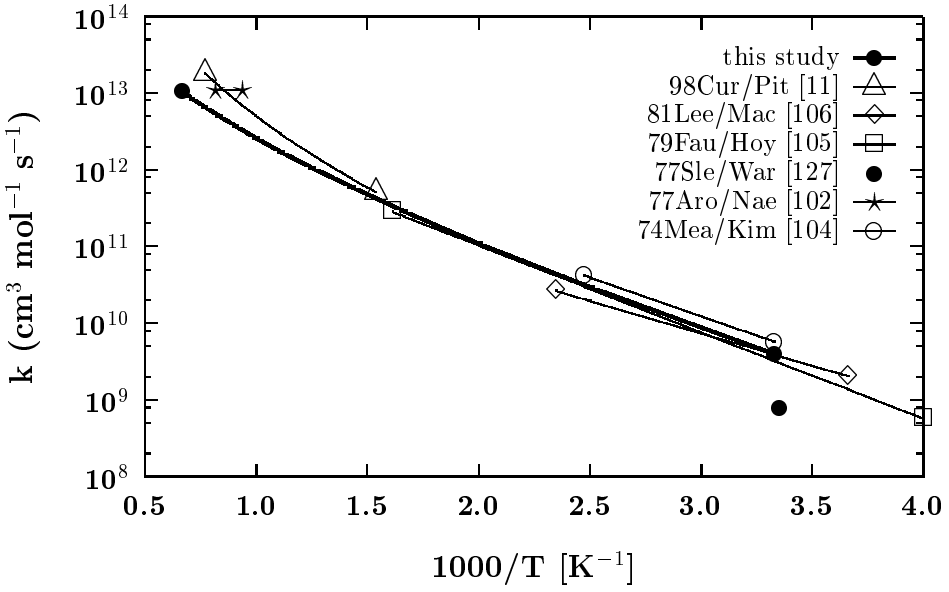

Figure 18: Arrhenius plot of rate constant expressions for $CH_3OCH_3 + \dot{H} = CH_3O\dot{C}H_2 + H_2$.

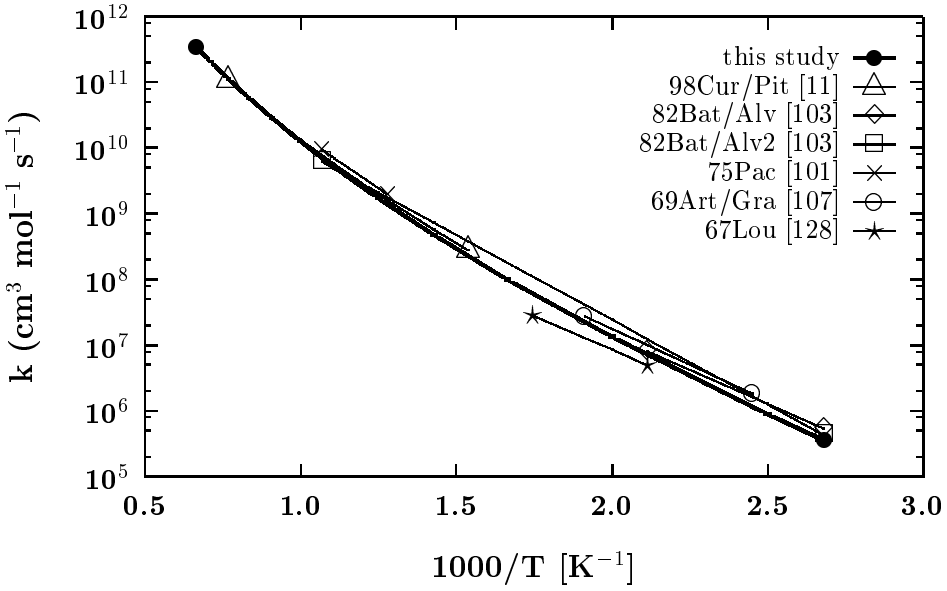

Figure 19: Arrhenius plot of rate constant expressions for $CH_3OCH_3 + \dot{C}H_3 = CH_3O\dot{C}H_2 + CH_4$.

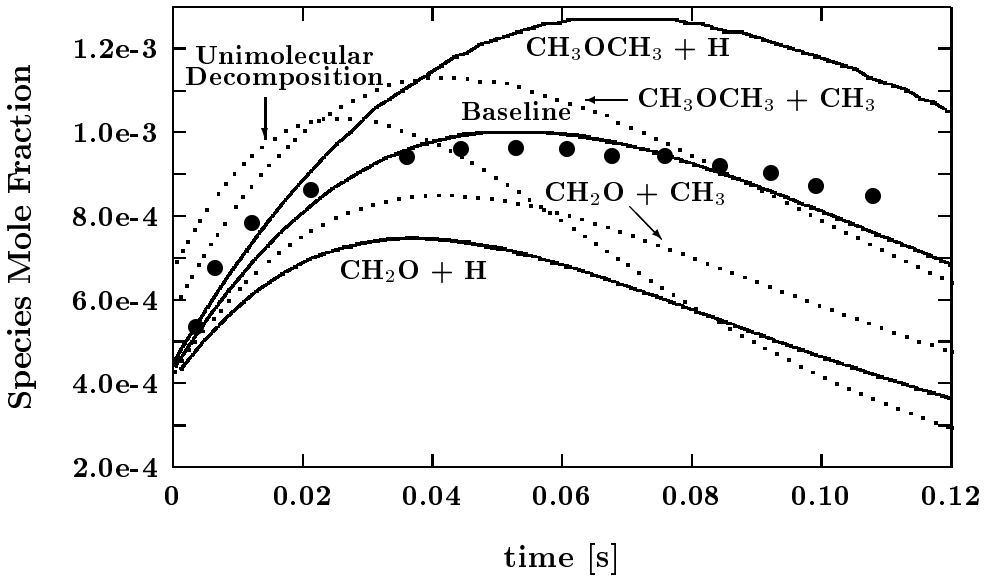

Figure 20: Sensitivity to formaldehyde formation for a flow reactor near-pyrolysis. 3740 ppm DME, P=1.0 atm, T=1118 K. • CH_2O. $\tau_{\text{offset}} = -0.015$ s.

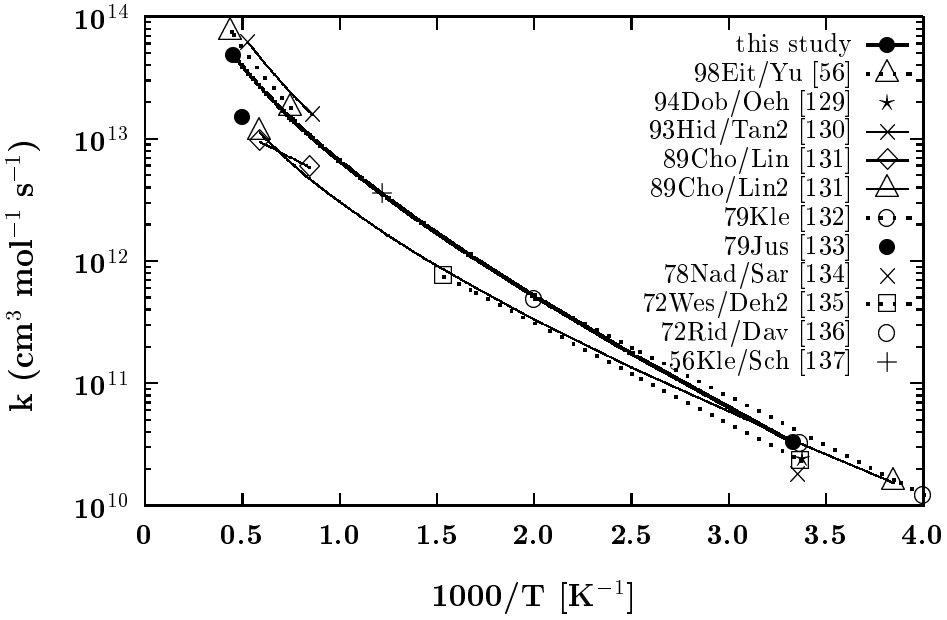

Figure 21: Arrhenius plot of rate constant expressions for $CH_2O + \dot{H} = H\dot{C}O + H_2$.

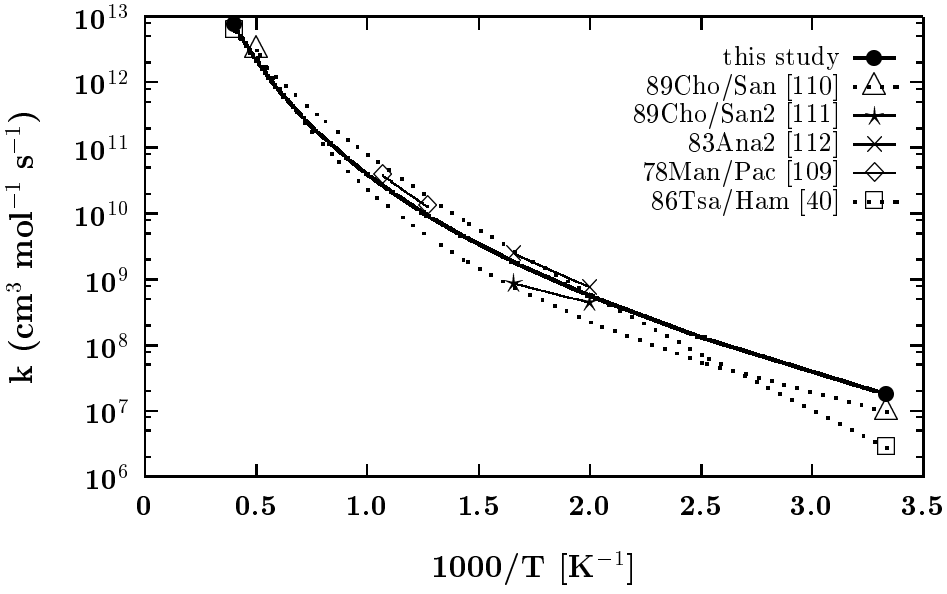

Figure 22: Arrhenius plot of rate constant expressions for $CH_2O + \dot{C}H_3 = H\dot{C}O + CH_4$.

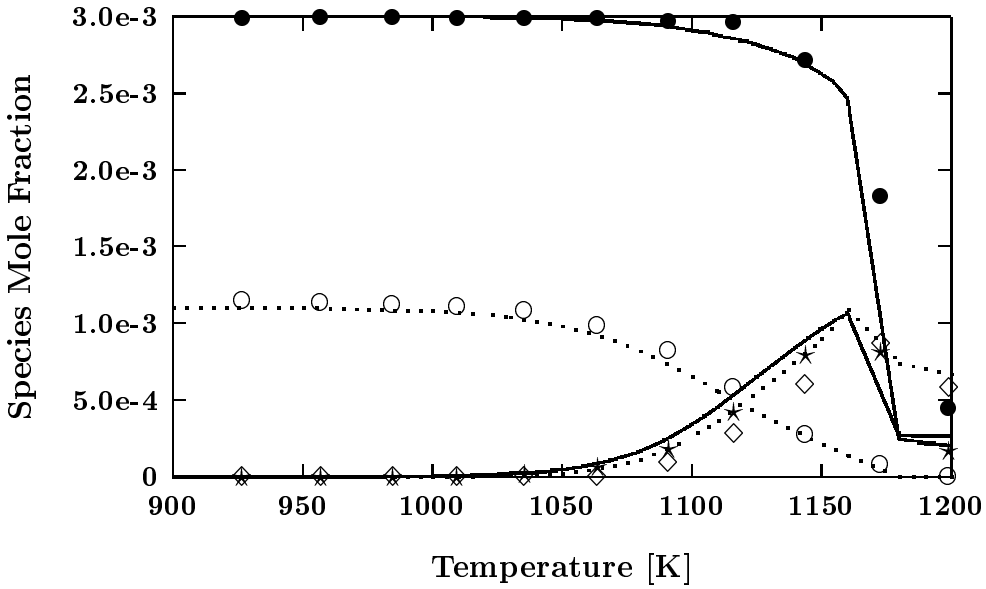

Figure 23: Experimental JSR results (symbols) [9] versus model predictions (lines) at 0.1% DME, $\phi = 1.0$, P=1 atm, τ=0.1 s. • O_2, ○ CH_3OCH_3, ⋆ H_2, and ◇ CO. Dotted lines correspond to open symbols.

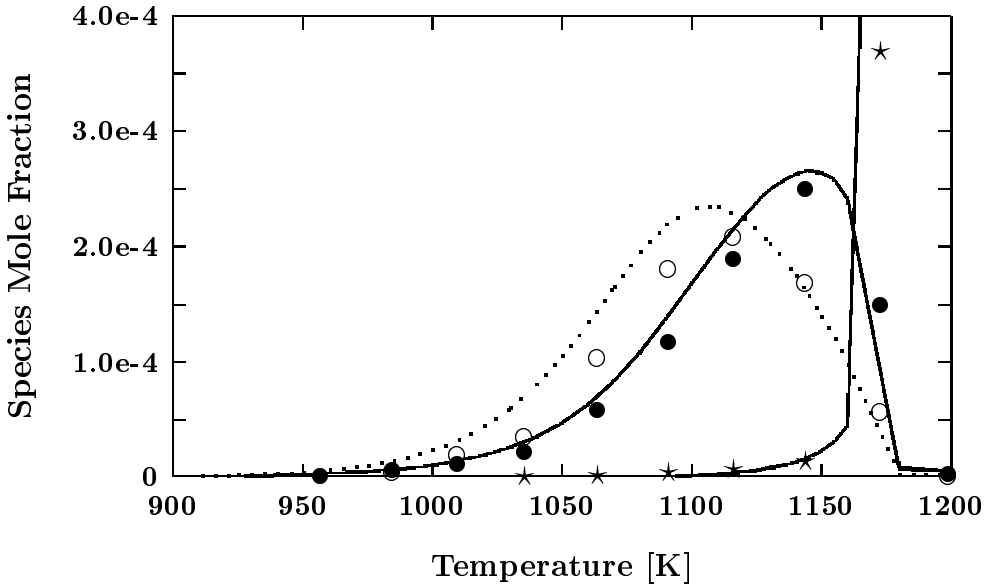

Figure 24: Experimental JSR results (symbols) [9] versus model predictions (lines) at 0.1% DME, $\phi = 1.0$, P=1 atm, τ=0.1 s. • CH_4, ○ CH_2O and ⋆ CO_2. Dotted lines correspond to open symbols.

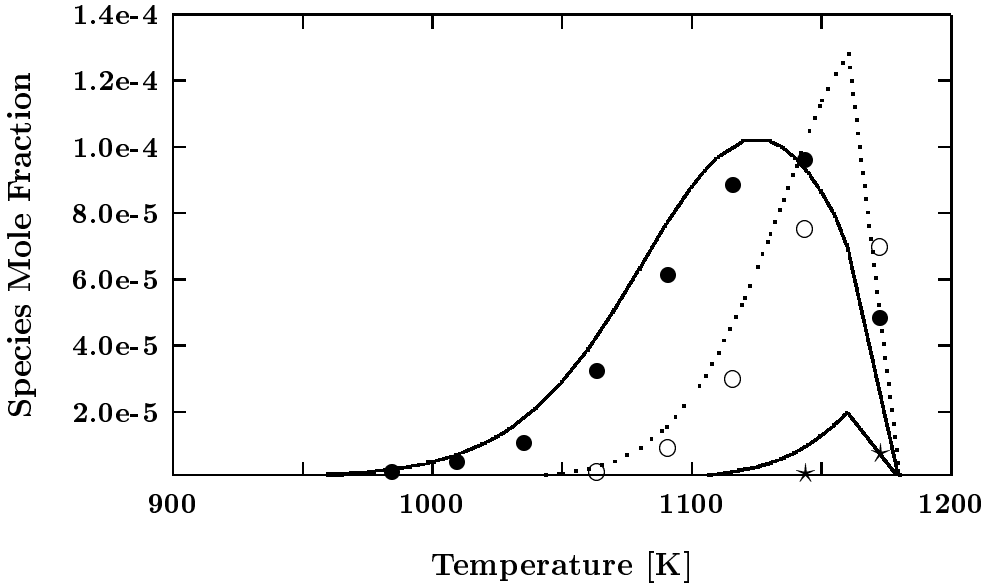

Figure 25: Experimental JSR results (symbols) [9] versus model predictions (lines) at 0.1% DME, $\phi = 1.0$, P=1 atm, τ=0.1 s. • C_2H_6, ○ C_2H_4 and ⋆ C_2H_2. Dotted lines correspond to open symbols.

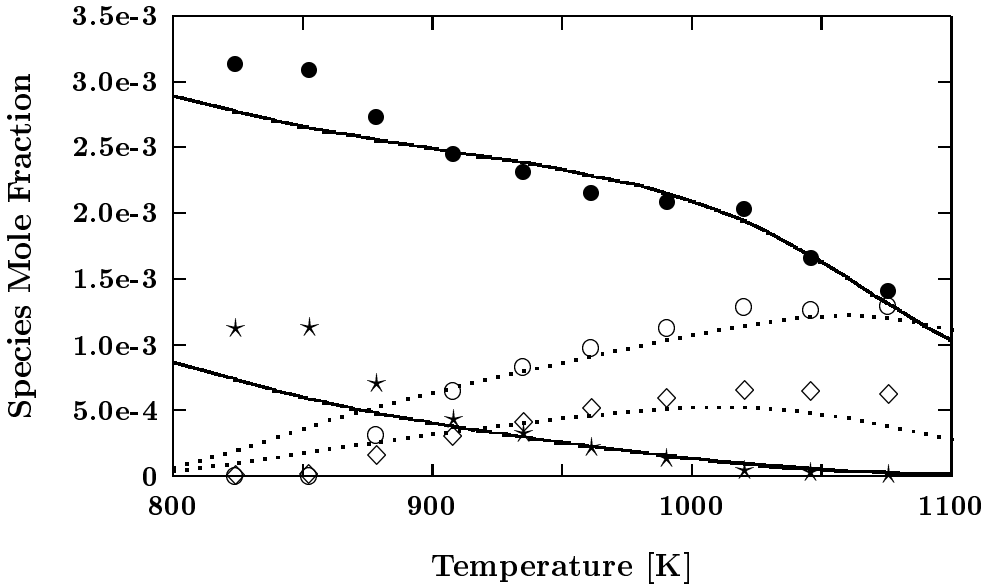

Figure 26: Experimental JSR results (symbols) [9] versus model predictions (lines) at 0.1% DME, $\phi = 1.0$, P=10 atm, τ=1 s. • O_2, ○ CO, ⋆ CH_3OCH_3, and ◇ H_2. Dotted lines correspond to open symbols.

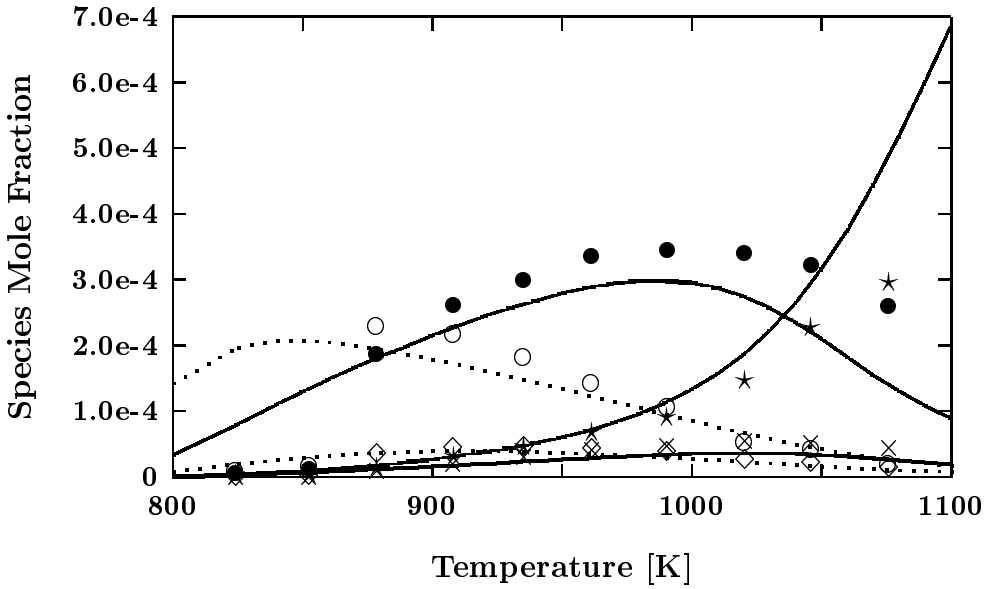

Figure 27: Experimental JSR results (symbols) [9] versus model predictions (lines) at 0.1% DME, $\phi = 1.0$, P=10 atm, τ=1 s. $\bullet$ CH_4, $\circ$ CH_2O, $\star$ CO_2, $\diamond$ C_2H_6, and $\times$ C_2H_4. Dotted lines correspond to open symbols.

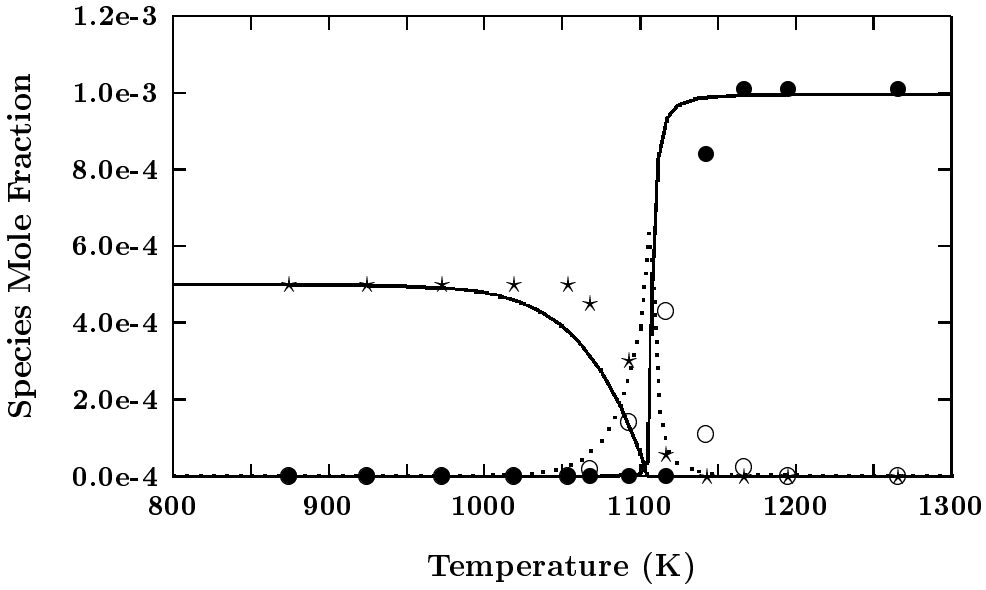

Figure 28: Experimental flow reactor (symbols) [13] versus model predictions (lines) at 500 ppm DME, 3000 ppm O_2, 3.34% H_2O, 96.3% N_2, P = 1.0 atm, $\tau = 188[K]/T$ (s). $\bullet$ CO_2, $\circ$ CO and $\star$ CH_3OCH_3. Dotted lines correspond to open symbols.

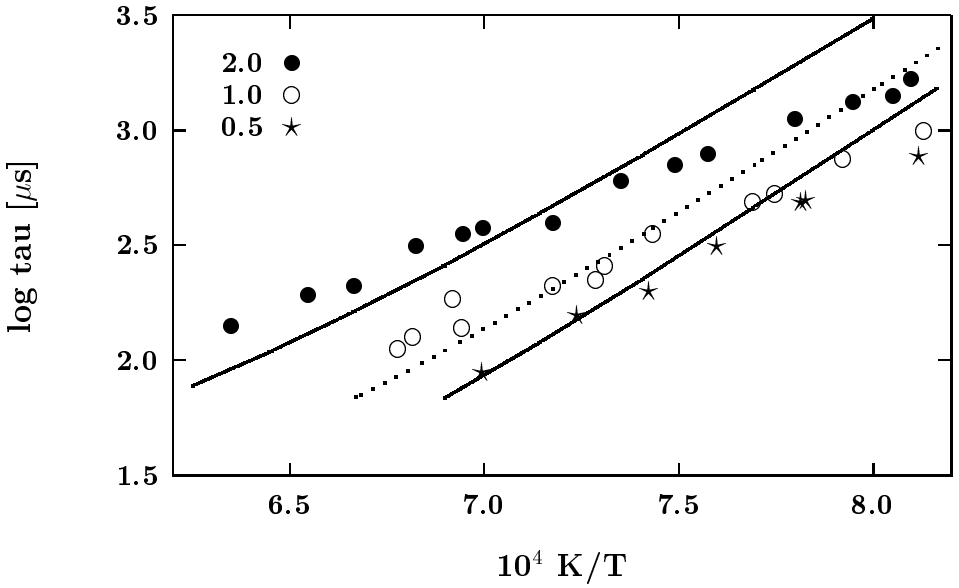

Figure 29: Effect of equivalence ratio on experimental shock-tube ignition delay times (symbols) [12] versus model predictions (lines) for 1.0% DME oxidation in argon at 3.5 bar. Dotted lines correspond to open symbols.

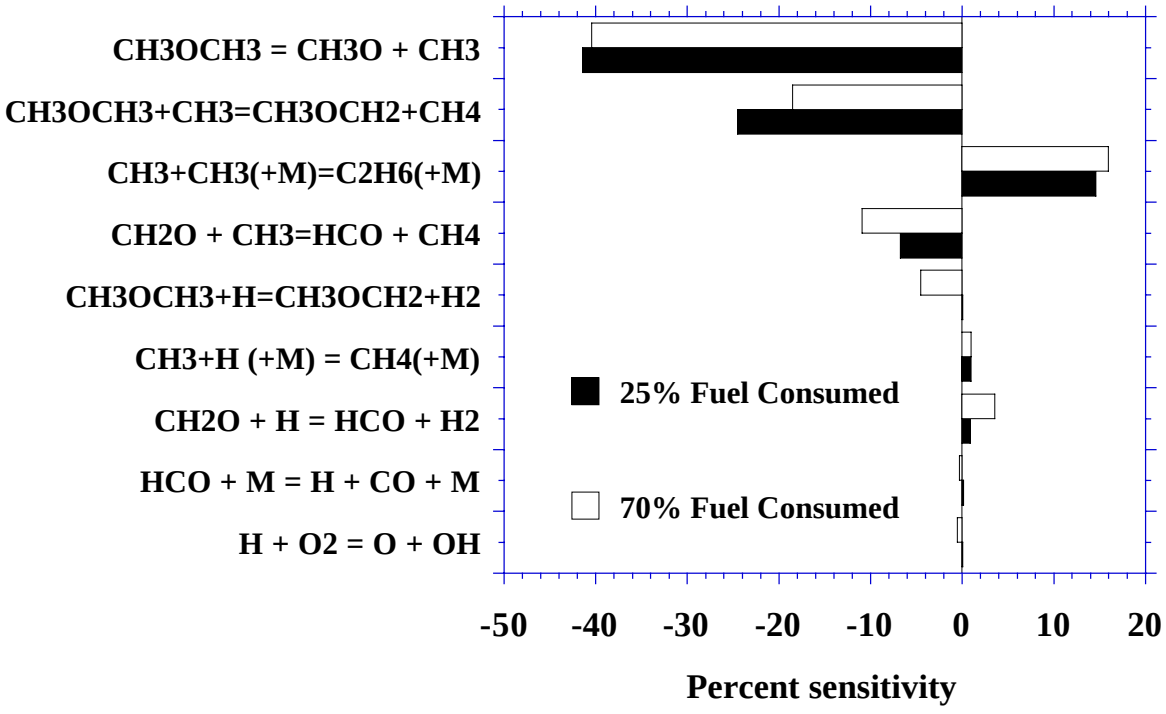

Figure 30: Sensitivity coefficients for time to percentage fuel consumed for a flow reactor near-pyrolysis. 3740 ppm DME, P=1.0 atm, T=1118 K.

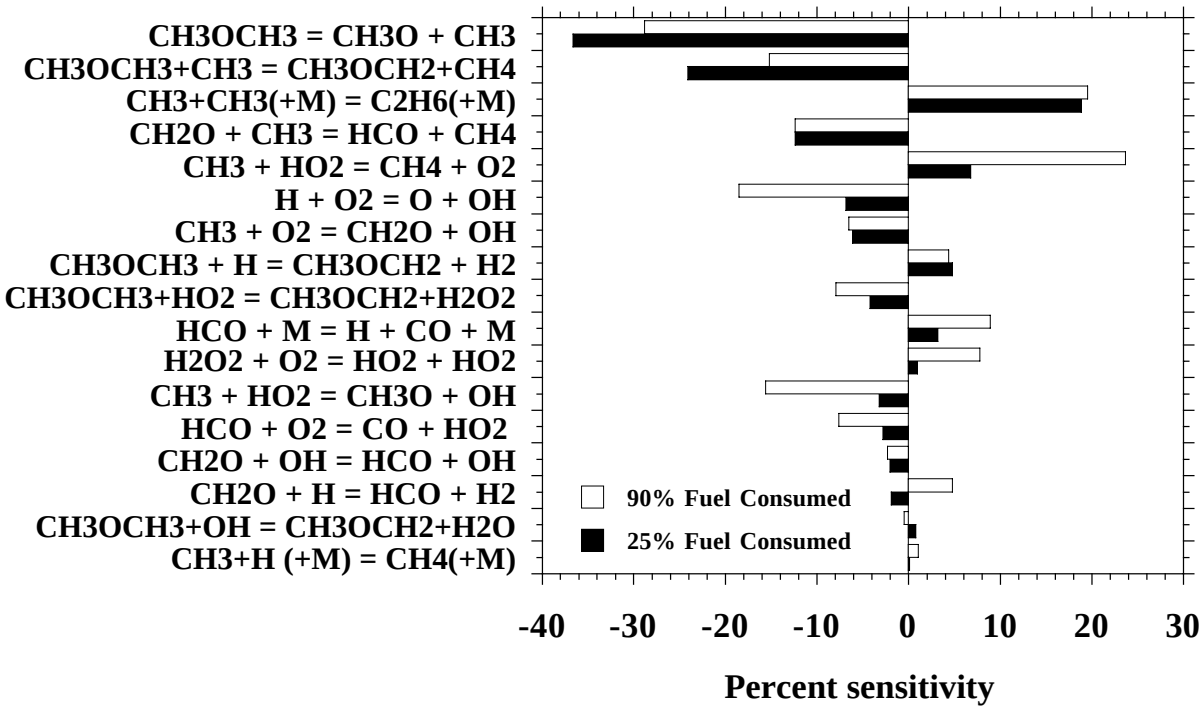

Figure 31: Sensitivity coefficients for time to percentage fuel consumed for a flow reactor oxidation. 5270 ppm DME, $\phi = 1.06$, P=1.0 atm, T=1084 K.